

AD-A151 882

FLOW OVER A BICONIC CONFIGURATION WITH AN AFTERBODY
COMPRESSION FLAP(U) AIR FORCE WRIGHT AERONAUTICAL LABS
WRIGHT-PATTERSON AFB OH J S SHANG ET AL. APR 84

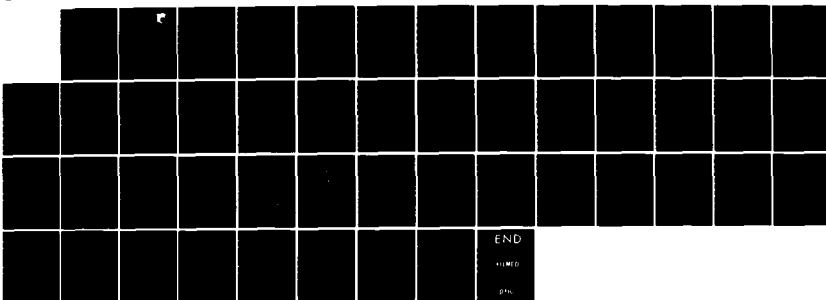
1/1

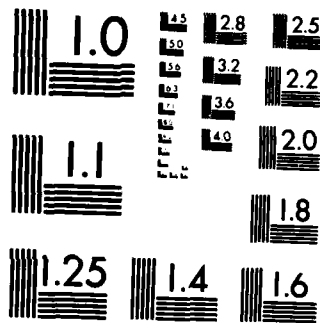
UNCLASSIFIED

AFWAL-TR-84-3059

F/G 20/4

NL





MICROCOPY RESOLUTION TEST CHART
NATIONAL BUREAU OF STANDARDS-1963-A

AD-A151 882

DMC FILE COPY

AFWAL-TR-84-3059



FLOW OVER A BICONIC CONFIGURATION WITH AN AFTERBODY COMPRESSION FLAP

J.S. Shang
R.W. MacCormack

Aerodynamics and Airframe Branch
Aeromechanics Division

April 1984

Final Report for Period January-April 1984

Approved for public release; distribution unlimited

FLIGHT DYNAMICS LABORATORY
AF WRIGHT AERONAUTICAL LABORATORIES
AIR FORCE SYSTEMS COMMAND
WRIGHT-PATTERSON AFB, OHIO 45433

SELECTED
MAR 27 1985
A

85 03 12 106

NOTICE

When Government drawings, specifications, or other data are used for any purpose other than in connection with a definitely related Government procurement operation, the United States Government thereby incurs no responsibility nor any obligation whatsoever; and the fact that the government may have formulated, furnished, or in any way supplied the said drawings, specifications, or other data, is not to be regarded by implication or otherwise as in any manner licensing the holder or any other person or corporation, or conveying any rights or permission to manufacture use, or sell any patented invention that may in any way be related thereto.

This report has been reviewed by the Office of Public Affairs (ASD/PA) and is releasable to the National Technical Information Service (NTIS). At NTIS, it will be available to the general public, including foreign nations.

This technical report has been reviewed and is approved for publication.

Project Manager
JOSEPH S. SHANG

Project Engineer

Tommy J. Kent
TOMMY J. KENT, Maj, USAF
Chief, Aerodynamics & Airframe Branch
Aeromechanics Division

FOR THE COMMANDER

Ralph W. Holm
RALPH W. HOLM, Col, USAF
Chief, Aeromechanics Division

"If your address has changed, if you wish to be removed from our mailing list, or if the addressee is no longer employed by your organization please notify AFWAL/FIMM, W-PAFB, OH 45433 to help us maintain a current mailing list".

Copies of this report should not be returned unless return is required by security considerations, contractual obligations, or notice on a specific document.

UNCLASSIFIED

SECURITY CLASSIFICATION OF THIS PAGE

REPORT DOCUMENTATION PAGE

1a. REPORT SECURITY CLASSIFICATION UNCLASSIFIED		1b. RESTRICTIVE MARKINGS	
2a. SECURITY CLASSIFICATION AUTHORITY		3. DISTRIBUTION/AVAILABILITY OF REPORT	
2b. DECLASSIFICATION/DOWNGRADING SCHEDULE		Approved for public release; distribution unlimited	
4. PERFORMING ORGANIZATION REPORT NUMBER(S) AFWAL-TR-84-3059		5. MONITORING ORGANIZATION REPORT NUMBER(S)	
6a. NAME OF PERFORMING ORGANIZATION FLIGHT DYNAMICS LABORATORY	6b. OFFICE SYMBOL (If applicable) AFWAL/FIMM	7a. NAME OF MONITORING ORGANIZATION FLIGHT DYNAMICS LABORATORY (AFWAL/FIMM)	
6c. ADDRESS (City, State and ZIP Code) FLIGHT DYNAMICS LABORATORY (AFWAL/FIMM) AF WRIGHT AERONAUTICAL LABORATORIES (AFSC) WRIGHT-PATTERSON AIR FORCE BASE, OH 45433		7b. ADDRESS (City, State and ZIP Code) FLIGHT DYNAMICS LABORATORY (AFWAL/FIMM) AF WRIGHT AERONAUTICAL LABORATORIES (AFSC) WRIGHT-PATTERSON AIR FORCE BASE, OH 45433	
8a. NAME OF FUNDING/SPONSORING ORGANIZATION	8b. OFFICE SYMBOL (If applicable)	9. PROCUREMENT INSTRUMENT IDENTIFICATION NUMBER	
8c. ADDRESS (City, State and ZIP Code)		10. SOURCE OF FUNDING NOS.	
		PROGRAM ELEMENT NO.	PROJECT NO.
		2307	N6
		TASK NO.	WORK UNIT NO.
		03	2307N603
11. TITLE (Include Security Classification) FLOW OVER A BICONIC CONFIGURATION WITH AN AFTERBODY COMPRESSION		14. DATE OF REPORT (Yr., Mo., Day) April 1984	
12. PERSONAL AUTHOR(S) FLAP J.S. Shang and R.W. MacCormack		15. PAGE COUNT 48	
16. SUPPLEMENTARY NOTATION			
17. COSATI CODES		18. SUBJECT TERMS (Continue on reverse if necessary and identify by block number)	
FIELD	GROUP	SUB GR.	
01	01		
19. ABSTRACT (Continue on reverse if necessary and identify by block number) Three-dimensional Navier-Stokes solutions were obtained for flow over a biconic configuration with an afterbody compression flap. The simulated flow was achieved for a Mach number of 7.97, a characteristic Reynolds number of 9.23 million and at a zero degree angle of attack. A comparative study was conducted using the vectorized MacCormack's explicit and implicit numerical schemes. Results from both the explicit and the implicit algorithms correctly yielded the detailed flow field structure and the heat transfer information in comparison with experimental data. However, the implicit numerical procedure exhibited a significant improvement in numerical efficiency over the explicit method. For fine mesh clustering near the solid body surface, necessary to resolve surface shear stress and heat transfer rates, the implicit scheme achieved an order of magnitude reduction in computing time.			
20. DISTRIBUTION/AVAILABILITY OF ABSTRACT UNCLASSIFIED/UNLIMITED <input checked="" type="checkbox"/> SAME AS RPT. <input type="checkbox"/> DTIC USERS <input type="checkbox"/>		21. ABSTRACT SECURITY CLASSIFICATION UNCLASSIFIED	
22a. NAME OF RESPONSIBLE INDIVIDUAL Joseph S. Shang		22b. TELEPHONE NUMBER (Include Area Code) (513) 255-2455	22c. OFFICE SYMBOL AFWAL/FIMM

FOREWORD

This report is the result of work carried on in the Computational Aerodynamics Group, Flight Dynamics Laboratory, Wright-Patterson Air Force Base, Ohio, by Dr J.S. Shang and Prof R.W. MacCormack from June 1983 to April 1984. During a part of this period, Prof MacCormack of the University of Washington was a visiting scientist at the Flight Dynamics Laboratory under Contract F33615-79-C-3030.

Accession For	
NTIS GRAET	
PTP TAB	
Document	
Justification	
Procurement	
Classification	
Availabilty	
Dist	
AII	



TABLE OF CONTENTS

<u>SECTION</u>		<u>PAGE</u>
I	INTRODUCTION.	1
II	ANALYSIS.	3
III	COORDINATE SYSTEM AND GRID GENERATION	7
IV	SOLVING SCHEME AND NUMERICAL PROCEDURE.	9
V	DISCUSSION OF RESULTS	14
VI	CONCLUSIONS	21
	REFERENCES.	22
	FIGURES.	24

LIST OF SYMBOLS

A, B	Jacobian of F, G ($\frac{\partial F}{\partial U}$, $\frac{\partial G}{\partial U}$)
c	Speed of sound
CFL	Stability coefficient
Def	Deformation tensor
D_A , D_B	Diagonal matrix
D	Van Driest's damping factor
e	Specific internal energy
F, G, H	Vector flux
h	Total enthalpy
\bar{I}	Identity matrix
K	Heat conductivity
L	Length scale of eddy viscosity model
M	Mach number
\bar{n}	Outward normal
p	Static pressure
P_T	Pitot pressure
Pr	Prandtl number 0.72
Pr_t	Turbulent Prandtl Number 0.9
q	Rate of heat transfer, $q = -k\nabla T$
r	Local radius of the biconic configuration
r_N	Blunt nose radius, 1.27 cm
Rey	Reynolds number based on running length
S	Running length originated from the nose tip
St	Stanton number, $St = \bar{n} \cdot \bar{q} / \rho_\infty u_\infty (h_\infty - h_b)$
T	Temperature

LIST OF SYMBOLS (Cont'd)

t	Time
\bar{U}	Dependent variables $U(\rho, \rho u, \rho v, \rho w, \rho e)$
u, v, w	Velocity components in Cartesian frame
u_ξ, u_η, u_ζ	Contravariant velocity components
x, y, z	Cartesian coordinates
y^+	The law of the wall variable, $y\sqrt{\rho w/\mu_b}$
α	$\alpha = (u^2 + v^2)/2$
β	$\beta = \gamma - 1$
γ	Specific heat ratio
δ_{ij}	Kronecker delta
ϵ	Eddy viscosity coefficient
ξ, η, ζ	Transformed coordinates
μ	Molecular viscosity coefficient
ρ	Density
τ	Stress tensor
ω	Vorticity vector
<u>Subscripts</u>	
∞	Freestream condition
o	Stagnation condition
b	Surface condition
$+$	Forward difference
$-$	Backward difference

SECTION I
INTRODUCTION

The ever widening application of computational aerodynamics to complex engineering problems makes the need for efficient numerical algorithms more apparent. In the past few years, several numerical algorithms have been developed¹, but additional research is still required to substantially improve numerical convergence rate, geometric adaptability and reliability of existing methods. Unfortunately, no attempt has been made to establish a commonly accepted criterion for the evaluation of the aforementioned requirements. One realizes that the magnitude of this undertaking is certainly beyond the scope of a single investigation. However, this information is vitally important to the application of computational aerodynamics in the design process. Therefore, the evaluation process is frequently forced to concentrate on the clearly defined issue of relative numerical efficiency. In the present effort, a comparative study was focused on MacCormack's explicit scheme and its implicit analogue. Specifically, the comparison was carried out by using the two procedures to solve a practical aerodynamic problem. The choice of solving schemes was based on the fact that the explicit scheme has frequently been used as a bench-mark^{3,4,5} for new algorithm development, and that the two investigated algorithms are easily adapted for vector processing.

The numerical simulation of flow over a biconic body with an afterbody compression flap (Figs. 1,2)* was obtained in this study. The computation was performed for flow with a nominal free stream Mach number of 7.97 and a characteristic Reynolds number of 9.23 million. This particular geometric configuration generates a wide variety of aerodynamic characteristics not

* Figures begin on page 24.

usually encountered in a single configuration. In particular, the flow field contains an enveloping bow shock, rapid expansions at the juncture of the biconic forebody and the sliced conical afterbody and finally an inviscid-viscous interaction around the afterbody compression flap. The solving procedure also offers the opportunity to evaluate the idea of segmented and overlapped computational domains^{1,6}. Basically, the problem was separated into two interdependent computational domains. The forebody was simulated by a simple axisymmetric numerical formulation. The comparative study of the explicit scheme and its implicit analogue was also limited to the axisymmetric forebody region. The more complex flow field around the afterbody was then analyzed using the full three-dimensional equations. The solution of the complete configuration is presented in composite form. The specific comparison with experimental data⁷ in terms of surface static pressure and heat transfer distributions as well as pitot pressure, Mach number and tangential velocity profiles will be given to verify the accuracy of the numerical simulation. The entire flow structure around the biconic configuration with the afterbody compression flap in terms of density contours, cross-flow velocity distribution and surface shear stress mapping will also be depicted. Finally, a detailed presentation on the comparative study of the explicit scheme and its implicit analogue will be delineated.

SECTION II
ANALYSIS

The time dependent, three-dimensional Navier-Stokes equations in mass-averaged variables and in the chain-rule conservation law form can be given as⁸

$$\frac{\partial \bar{U}}{\partial t} + (\xi_x, \xi_y, \xi_z) \begin{pmatrix} F_\xi \\ G_\xi \\ H_\xi \end{pmatrix} + (n_x, n_y, n_z) \begin{pmatrix} F_n \\ G_n \\ H_n \end{pmatrix} + (\zeta_x, \zeta_y, \zeta_z) \begin{pmatrix} F_\zeta \\ G_\zeta \\ H_\zeta \end{pmatrix} = 0 \quad (1)$$

The dependent variables are $\bar{U}(\rho, \rho u, \rho v, \rho w, \rho e)$. The flux vectors, F, G, and H are simply the Cartesian components of the continuity, momentum and energy equations. The axisymmetric formulation is but a subset of the governing equations.

$$F = \begin{pmatrix} \rho u \\ \rho u^2 - \tau_{xx} \\ \rho u v - \tau_{xy} \\ \rho u w - \tau_{xz} \\ \rho e u - \gamma \left(\frac{\mu}{Pr} + \frac{\epsilon}{Pr_t} \right) \frac{\partial e}{\partial x} - (u \tau_{xx} + v \tau_{xy} + w \tau_{xz}) \end{pmatrix} \quad (2)$$

$$G = \begin{pmatrix} \rho v \\ \rho u v - \tau_{yx} \\ \rho v^2 - \tau_{yy} \\ \rho v w - \tau_{yz} \\ \rho e v - \gamma \left(\frac{\mu}{Pr} + \frac{\epsilon}{Pr_t} \right) \frac{\partial e}{\partial y} - (u \tau_{yx} + v \tau_{yy} + w \tau_{yz}) \end{pmatrix} \quad (3)$$

$$H = \begin{pmatrix} \rho w \\ \rho u w - \tau_{zx} \\ \rho v w - \tau_{zy} \\ \rho w^2 - \tau_{zz} \\ \rho e w - \gamma \left(\frac{\mu}{Pr} + \frac{\epsilon}{Pr_t} \right) \frac{\partial e}{\partial z} - (u \tau_{zx} + v \tau_{zy} + w \tau_{zz}) \end{pmatrix} \quad (4)$$

where, the component of shear stress is defined by

$$\tau_{ij} = (\mu + \epsilon) (\text{Def } \bar{u})_{ij} - \left[\frac{2}{3} (\mu + \epsilon) \nabla \cdot \bar{u} + p \right] \delta_{ij} \quad (5)$$

The closure of this system of equations is achieved by introducing the Baldwin-Lomax turbulence model⁹ with a minor modification⁸ and by assigning a turbulent Prandtl number of 0.9. Specifically, the two-layer eddy viscosity model is given by

Inner region:

$$\epsilon = \rho (0.4LD)^2 |\omega| \quad (6)$$

In the present formulation, the vorticity of the flow ω , the Van Driest damping factor D , and the scaling length L are given as follows

$$\omega = \frac{1}{2} \nabla \times \bar{u} \quad (7)$$

$$D = 1 - \exp \left[- \frac{\rho_b |\omega_b|}{\mu_b} \right]^{1/2} L/26 \quad (8)$$

$$L = [(x-x_b)^2 + (y-y_b)^2 + (z-z_b)^2]^{1/2} \quad (9)$$

Outer region:

$$\epsilon = 0.0336 \rho F_{\text{wake}} / [1 + 5.5(0.3L/L_{\text{max}})^6] \quad (10)$$

The wake function, F_{wake} is the minimum value of the two following expressions at any point in space.

$$F_{\text{wake}} = L_{\text{max}} \cdot F_{\text{max}} \quad (11)$$

$$F_{\text{wake}} = 0.25 \cdot L_{\text{max}} \cdot (u^2 + v^2 + w^2)_{\text{max}} / F_{\text{max}} \quad (12)$$

In the present analysis, L_{max} is the value of the length scale where $F = LD|\omega|$ reaches its maximum value within the turbulent shear layer. The system of equations is formally closed with Sutherland's equation for molecular viscosity and the equation of state for a perfect gas.

Since a composite solution obtained by overlapping computational domains for the investigated problem was performed, different initial and boundary conditions were imposed for each subproblem. However, since these conditions are quite similar, they will be discussed together. The initial condition for the forebody solution consisted of freestream values for all field points excluding the surface nodes.

$$\bar{U}(0, \xi, n, \zeta) = \bar{U}_\infty \quad (13)$$

The initial condition of the three-dimensional afterbody solution is described in part by the forebody calculation. The overlapping station is located at a distance of 45.5 radii downstream of the blunt nose. The initial value assigned to the overlapping surface also serves as the upstream boundary condition for the afterbody calculation. This is the only link between the forebody and the afterbody solutions.

On the solid body contour, the no-slip condition for velocity components, the isothermal condition for temperature to duplicate experimental conditions, and the ortho-isobaric condition for pressure are imposed. The value of surface density is deduced from the equation of state.

$$u, v, w = 0 \quad (14)$$

$$T_b = 311.3^\circ K \quad (15)$$

$$\bar{n} \cdot \nabla p = 0 \quad (16)$$

where the outward normal of the body oriented coordinate is simply,
 $\bar{n} = \nabla n / \| \nabla n \|$.

Since the detached bow shock wave isolates the interacting flow domain, the far field condition requires that the flow remain unperturbed.

$$\bar{U}(t, \xi, 1, \zeta) = \bar{U}_\infty \quad (17)$$

For the afterbody computation, the present analysis takes advantage of the

property of symmetry with respect to the y axis (Fig. 3). Only half of the cross-flow plane is evaluated. A reflection condition is applied which insists that the ζ component of velocity be equal to zero on the plane of symmetry.

$$\frac{\partial U}{\partial \zeta} = 0, w = 0 \quad (18)$$

Finally, the usual no-change condition is imposed at the downstream boundary for each computational domain. This system of boundary conditions is known to be well-posed and stable for the supersonic problem.

SECTION III

COORDINATE SYSTEM AND GRID GENERATION

The numerical generation of body-oriented coordinates is straightforward. The adopted method is the homotopy scheme¹⁰. Basically, it is an interpolation procedure between grid control surfaces. Once the inner and the outer surface are given, any number of mesh surface points is controlled by an exponential stretching function. For turbulent flow this stretching is nearly optimum in describing the logarithmic velocity profile. The mesh formulation is given by

$$y = y_o \left(\frac{e^{kn} - 1}{e^k - 1} \right) + y_i \left(1 - \frac{e^{kn} - 1}{e^k - 1} \right) \quad (19)$$

$$z = z_o \left(\frac{e^{kn} - 1}{e^k - 1} \right) + z_i \left(1 - \frac{e^{kn} - 1}{e^k - 1} \right) \quad (20)$$

where $0 < \eta < 1$. The exponent of the stretching function is uniquely determined by the minimum distance between the body and the immediately adjacent coordinate surface, and by the number of points used. Additional mesh clustering around the bow shock wave is generated by increasing the total number of nodes in η direction by four in this region and subdividing the mesh previously generated using the logarithmic coordinate surfaces locally near the bow shock (Figure 2 and 3). For the baseline case of computation, the calculated value of the exponent k is 4.820. The finest outward normal distance from the body surface is assigned a value of 0.00305 cm in the blunt nose region. However, the grid spacing increases four-fold in the aft portion of the biconic forebody, where the law of the wall variable y^+ assumes a value of 5.901.

For the forebody calculation, the outer coordinate line, $\eta=1$, is described by a curve consisting of a circle and a parabola matched to closely approximate the bow shock wave. Care is also exercised to ensure that the generated

coordinates are nearly orthogonal. In order to achieve a systematic comparative study, various mesh distributions are generated by reducing the Δn value (inversely proportional to the total number of nodes chosen) and retaining the exponent k at the fixed value of 4.820. In this manner, the coordinate systems are affine and the computational domains are unaltered. The streamwise numerical resolution is also evaluated by using two different streamwise mesh systems which comprise (62x40) nodes and (90x40) nodes, respectively.

The three-dimensional afterbody calculation, the coordinate system is constructed by a series of consecutive axial cross sections evenly spaced to achieve optimal numerical resolution. The first thirteen streamwise step-spacings upstream of the compression flap have the value of 0.859 cm, which is less than half the boundary-layer thickness at the overlapping plane. A finer streamwise step size (0.4276 cm) is used for the rest of the streamwise stations. The body geometry variation is relatively mild with two sliced surfaces on the top and bottom of the conic body and a 20° compression flap. Therefore, only 38 circumferential points were used to define the cross-sections. All the mesh points have an even angular displacement of 5°. The first two and the last two arrays of mesh points were astriding the plane of symmetry. A total of (33, 40, 38) mesh points were used for the afterbody calculation. In Figure 3, four typical cross-sectional grid point distributions are presented.

SECTION IV
SOLVING SCHEME AND NUMERICAL PROCEDURE

The well-known MacCormack's explicit unsplit algorithm is used as the basis of the present comparative study. The unsplit scheme can be easily coded to exploit computer architecture resulting in a minimum amount of data movement to and from the memory unit of vector processors. The explicit scheme, however, is conditionally stable; the inviscid allowable time increment for arbitrary coordinates have been derived and can be given by⁸

$$\Delta t_{CFL} = \text{CFL} / \{u_\xi / \Delta \xi + u_\eta / \Delta \eta + u_\zeta / \Delta \zeta + c[(\frac{\xi_x}{\Delta \xi} + \frac{\eta_x}{\Delta \eta} + \frac{\zeta_x}{\Delta \zeta})^2 + (\frac{\xi_y}{\Delta \xi} + \frac{\eta_y}{\Delta \eta} + \frac{\zeta_y}{\Delta \zeta})^2 + (\frac{\xi_z}{\Delta \xi} + \frac{\eta_z}{\Delta \eta} + \frac{\zeta_z}{\Delta \zeta})^2]^{1/2}\} \quad (21)$$

where the contravariant velocity components are defined as

$$u_\xi = \xi_x u + \xi_y v + \xi_z w \quad (22)$$

$$u_\eta = \eta_x u + \eta_y v + \eta_z w \quad (23)$$

$$u_\zeta = \zeta_x u + \zeta_y v + \zeta_z w \quad (24)$$

Since this stability condition for time step size does not contain viscous terms, the maximum allowable time increment for the actual computation must be determined numerically. For the present analysis, the highest and most consistent CFL number is 0.8 and is used throughout as the criterion for the numerical efficiency study.

The detailed description of MacCormack's implicit algorithm is documented in reference 3 and therefore will not be elaborated on here. The implicit algorithm can be directly implemented into the existing code, with the basic

idea being to convey the locally determined solution evolution globally in a stable manner. The implicit propagation of local solution changes in time are given by the following equation.

$$(I + \Delta t \frac{\partial A^*}{\partial \eta} + \Delta t \frac{\partial B^*}{\partial \zeta}) \frac{\partial \bar{U}^{n+1}}{\partial t} = \frac{\partial \bar{U}^n}{\partial t} \quad (25)$$

where A and B are the Jacobians of F and G with respect to the dependent variable \bar{U} . The notation in the (A^*, B^*) above expression simply indicates that the spatial derivative also operates on the time derivative $\frac{\partial \bar{U}^{n+1}}{\partial t}$. The numerical procedure is first performed for the explicit predictor sweep, then followed by the implicit sweep for the nodes where the time-step exceeds the CFL limit locally. This procedure is repeated for the corrector sweep. The implicit differencing operator is parallel to that of the explicit differencing operator. The alternative one-sided difference approximates the first derivative and the second derivative are centrally differenced.

$$(I - \Delta t \frac{\Delta_+ |A|}{\Delta \eta}) (I - \Delta t \frac{\Delta_+ |B|}{\Delta \zeta}) \delta \bar{U}^{n+1} = \Delta \bar{U}^n \quad (26)$$

$$(I + \Delta t \frac{\Delta_- |A|}{\Delta \eta}) (I + \Delta t \frac{\Delta_+ |B|}{\Delta \zeta}) \delta \bar{U}^{n+1} = \Delta \bar{U}^n \quad (27)$$

where

$$\delta \bar{U}^{n+1} = \Delta t \frac{\partial \bar{U}^{n+1}}{\partial t}$$

$$\Delta \bar{U}^n = \Delta t \frac{\partial \bar{U}^n}{\partial t}$$

The matrices $|A|$ and $|B|$ are the matrices with positive eigen values and are related to the Jacobians A and B . Specifically, the matrices A and B can be expressed by it's diagonalized matrices and the similar transformation matrices in terms of the general coordinates

$$A = S_n^{-1} D_A S_n \quad (28)$$

$$B = S_\zeta^{-1} D_B S_\zeta \quad (29)$$

where

$$S_n^{-1} = \begin{bmatrix} 1 - \alpha\beta/c^2 & \beta u/c^2 & \beta v/c^2 & -\beta/c^2 \\ (\alpha\beta - u_n c)/2 & (\eta_x c - \beta u)/2 & (\eta_y c - \beta v)/2 & \beta/2 \\ -v_n/\rho & -\eta_y/\rho & \eta_x/\rho & 0 \\ (u_n c + \alpha\beta)/2 & -(\eta_x c + \beta u)/2 & (\eta_y c + \beta v)/2 & \beta/2 \end{bmatrix} \quad (30)$$

$$S_n^{-1} = \begin{bmatrix} 1 - \alpha\beta/c^2 & \beta u/c^2 & \beta v/c^2 & -\beta/c^2 \\ (\alpha\beta - u_n c)/2 & (\eta_x c - \beta u)/2 & (\eta_y c - \beta v)/2 & \beta/2 \\ -v_n/\rho & -\eta_y/\rho & \eta_x/\rho & 0 \\ (u_n c + \alpha\beta)/2 & -(\eta_x c + \beta u)/2 & (\eta_y c + \beta v)/2 & \beta/2 \end{bmatrix} \quad (31)$$

$$D_A = \begin{bmatrix} u_n & 0 & 0 & 0 \\ 0 & u_n + c & 0 & 0 \\ 0 & 0 & u_n & 0 \\ 0 & 0 & 0 & u_n - c \end{bmatrix} \quad (32)$$

$$D_B = \begin{bmatrix} u_\zeta & 0 & 0 & 0 \\ 0 & u_\zeta + c & 0 & 0 \\ 0 & 0 & u_\zeta & 0 \\ 0 & 0 & 0 & u_\zeta - c \end{bmatrix} \quad (33)$$

The flux change in either the η or the ζ directions are easily given as $S_\eta^{-1} \partial \bar{U}$, and $S_\zeta^{-1} \partial \bar{U}$, respectively.

Since the procedure is implicit, the treatment of boundary conditions is critical to further improve the rate of numerical convergence. At this writing, the transmitted flux change at the $\zeta = 0$ boundary is swept immediately back into the flow field, leaving no corrections to be performed later. However, the present procedure stored the transmitted flux received at the inner boundary ($\eta = 0$) during the predictor implicit sweep, and then later sweeps it back out during the corrector step. Although flux changes are rigorously conserved, there is a time lag. The implementation of implicit boundary condition is a vital area for future research and continuous efforts are currently still being undertaken.

For the investigated case, the static pressure jumped seventy-four fold across the bow shock wave enveloping the blunt nose region. Numerical damping was required to suppress numerical oscillations, therefore, fourth-order pressure damping terms¹¹ are used in the present analysis. The magnitude of the artificial viscosity-like terms are restricted to a value not to exceed 0.5.

$$\Delta t \Delta \eta^3 [|u_\eta| + (\eta_x^2 + \eta_y^2 + \eta_z^2)^{1/2} c] \frac{1}{p} \left| \frac{\partial^2 p}{\partial \eta^2} \right| \leq 0.5$$

A transient damping term representing a measure of the change in entropy primarily induced by viscous dissipation is also used to maintain stability³.

$$|\delta p/c^2 - \delta \rho| / \left(\frac{\Delta t}{\Delta \eta} \right) \left(\frac{\gamma-1}{\gamma} \right) \rho$$

This additional precautionary measure vanishes when the asymptotic steady state solution is reached.

The aforementioned implicit numerical procedure results in matrix equations to be solved that are either upper or lower block bidiagonal. Since no recurrent relationship is required to invert the system of equations, the vectorization of the implicit procedure is easily achieved. The implicit calculation needs only twenty-three percent more CPU time to process the data than the explicit scheme. The additional computing resources required for the implicit code are nearly identical for either scalar or vector processors. Finally, the numerical convergence criterion for the present analysis is defined as a change in the Stanton number of less than one percent per one half of a characteristic time. The time scale is the period for a fluid particle to travel from the upstream to downstream boundaries of the computational domain at the freestream velocity.

SECTION V

DISCUSSION OF RESULTS

The present results will be discussed in two parts. In the first topic, the comparative study of the explicit method and it's implicit analogue applied to simulate the biconic forebody is presented. A brief discussion is also included on the relative numerical efficiency between the full and the parabolized Navier-Stokes solutions for the investigated configuration. The rest of the presentation concentrates on the delineation of the detailed flow structure around the afterbody with a 20° compression flap and a sliced conic shape. All of the comparisons and validation are accompanied by experimental data collected under identical conditions.

The comparative study of MacCormack's explicit scheme and it's implicit counterpart is focused on the axisymmetric forebody from the following rational. First, the major attraction of using an implicit scheme to simulate a given problem is that of the favorable stability characteristic of the implicit scheme leading to a decrease in the required computing resources. In principle, the implicit scheme always requires more arithmetic operations than the explicit method to advance a given time step. Thus the favorable allowable time step size must overwhelm the conditionally stable explicit scheme to gain an overall advantage in data processing time. For most aerodynamics applications, the mesh refinement for the viscous dominated region usually is not required along more than two coordinate directions^{4,5,8,9}. Therefore, the implicit procedure may not need to be implemented for all the coordinates in order to achieve the most efficient results. Second, the forebody numerical simulation offers a severe challenge for any numerical algorithm in simulating the strong bow shock wave around the rapidly changing curvature of the blunt nose and the

resulting rapid flow expansion that follows. Finally, each transformed coordinate must rotate 90° to accomodate the definition of the body.

In the following table, the data processing rate and the total CPU time used to meet the convergence criterion mentioned eariler are given. It is observed that the ratio of data processing rates between the explicit scheme and the implicit scheme remains nearly identical, regardless of whether the codes were performed on scalar or vector processors. This is a clear indication that MacCormack's implicit scheme is more readily vectorized than other implicit methods which require tridiagonal block matrix inversion. This advantage in application is critical for large scale data processing at present. The allowable time step size for the implicit algorithm is recorded for a stringent application standard; the accepted CFL number must be sustained until the evolving solution meets the convergence criterion. No prolonged relaxation period was allocated to diminish the larger temporal truncation errors. Most important of all only the practical fine grid spacing adjacent to the surface sufficient to resolve the heat transfer was used. In the eddy viscosity formulation, the laminar sublayer thickness is normalized by the law of the wall variable y^+ with a value of 26. Based on early investigations of strong inviscid-viscous interactions, a y^+ value less than 10 is usually adequate to resolve the shear stress and heat transfer information^{12,13}. Further refinement of the mesh adjacent to the surface would yield a higher CFL value, but may not be cost effective. Nevertheless, for the case of $y^+ = 5.901$, the implicit procedure can consistently process data at a time step value 4.125 times higher than the explicit scheme. The net total computing resources savings amounts to a factor of 3.3 in comparison with the explicit procedure. As the surface mesh spacing reduces to correspond

to a y^+ value of 3, the implicit scheme performs at a consistent CFL value of 16.1. The computational resource savings increases to an impressive factor of 10.09. The difference in predicting the Stanton number distribution between the fine ($y^+ = 3$) and the coarse ($y^+ = 5.9$) mesh solution is less than one percent. For our purpose, the numerical results are considered identical.

Algorithm	Mesh Spacing	y^+	Computer	DPR	Total CPU	$\frac{\Delta t}{\Delta t_{CFL}}$
Explicit	(62,40)	5.9	CYBER 175	6.1×10^{-4}	15123.0	1.0
Implicit	(62,40)	5.9	CYBER 175	7.5×10^{-4}	4582.7	4.125
Explicit	(90,40)	5.9	CRAY 1S	1.78×10^{-5}	641.9	1.0
Implicit	(90,40)	5.9	CRAY 1S	2.21×10^{-5}	194.5	4.110
Explicit	(62,40)	5.9	CRAY 1S	1.72×10^{-5}	426.00	1.0
Implicit	(62,40)	5.9	CRAY 1S	2.13×10^{-5}	129.10	4.110
Explicit	(62,41)	3.0	CRAY 1S	1.72×10^{-5}	1864.2	1.0
Implicit	(62,41)	3.0	CRAY 1S	2.43×10^{-5}	142.0	16.1

The afterbody calculation was accomplished using a (33,40,48) mesh system to describe the flow field around the 20° compression flap. The initial condition for the afterbody simulation was prescribed by the value of the overlapping plane, which is a much better guess than the forebody initial condition. At a data processing rate of 6.1×10^{-5} seconds, the numerical solution converged after 2,374.8 seconds CPU time. On the other hand, the numerical solutions generated by various parabolized Navier-Stokes codes^{14,15} of a similar configuration (10° flap) required a range of 291 to 537 seconds of computer time on a CARY computer¹⁶. The numerical efficiency of parabolized Navier-Stokes procedures is impressive. However, the cited CPU time excludes the Navier-Stokes calculations of the blunt nose which these procedures need as an initial condition. The difference in total computing resources for the

entire numerical simulation between the full Navier-Stokes and the parabolized Navier-Stokes equations is less than an order of magnitude.

In Figure 4, the comparison of the surface pressure distributions on the forebody reveals excellent agreement. The solutions by the explicit and implicit methods are indistinguishable. The maximum discrepancy between experimental data and calculations is limited to less than four percent. The Stanton number distributions and the accompanying data is given in Figure 5. The over-all agreement between data and the calculations is very good. The maximum discrepancy is near the high expansion and recompression region where laminar turbulent transition might occur. Since a tripping device was used for the experimental measurement to ensure a fully developed turbulent flow, the numerical simulation would not be expected to duplicate the local phenomenon. However, downstream of the junction of the biconic configuration, agreement between the experimental data and the calculation is excellent. The prediction by the Navier-Stokes equations indicates a comparable result to that of the parabolized Navier-Stokes equations¹⁶. In this comparison, the implicit solution reveals merely a 1.6 percent higher value in Stanton number evaluation than the explicit result. This is also the maximum disparity between the implicit and the explicit solutions investigated.

The comparisons of pitot pressure and tangential velocity profiles are given in Figures 6 and 7, respectively. The detailed flow field survey was performed at 41.5 radii downstream of the blunt nose in the meridian plane. The agreement between experimental data and the calculations is very good. Again, differences between the solutions achieved by the explicit method and the implicit scheme are indistinguishable. The major deviation between

the experimental data and the numerical solutions is confined within the entropy layer induced by the bow shock curvature in the stagnation region, and in the definition of the shock wave. This is a fundamental short coming of a shock capturing scheme.

In order to better organize the discussion of the three-dimensional afterbody calculation, the density contour of the entire biconic configuration with a 20° compression flap in the meridian plane is depicted in Figure 8. The enveloping bow shock wave, the rapid expansions downstream of the stagnation region and the conic junction and finally the coalesced compression shock waves over the flap are clearly indicated. In the lower half of the meridian plane at the end of the conical section, a continuous expansion is also observed over the bottom sliced surface. To give a proper perspective of the three-dimensional flow field structure, four cross-sectional density contours are given in Figure 9. The systematic development of the expansion zone over the slice and compression flap is obvious. The most interesting feature is that the coalescing shock wave system over the flap is isolated by the expansion domain above the slice. Therefore, the distortion of the enveloping bow shock is rather limited.

The surface pressure distributions on the body surface in the meridian plane are presented in Figure 10. The agreement on both the upper and the lower surfaces are excellent. A good agreement also is reached for the circumferential Stanton number distributions between data and calculation in two streamwise locations, when experimental measurements are available (Figure 11). The angular displacement, defined to be zero in the upper meridian plane, increases in the clockwise direction until the lower meridian plane is reached. The streamwise Stanton number distribution is also calculated and the agreement with data is very good.

Four pitot pressure surveys, one upstream of the location of the compression flap ($x/r_N = 49.01$), one roughly one boundary-layer thickness downstream of the flap junction and two locations near the end of the compression flap are illustrated in Figure 12. The last survey data set was collected in the model centerline and near the spanwise edge of the compression flap. Very good agreement between data and the calculation is observed. The maximum deviation is estimated to be confined within a few percent and is mostly limited to the domain of the entropy layer and the definition of the bow shock. The peak values of the pitot pressure around the coalescing shock wave are predicted with increasing accuracy in the fine mesh distribution near the body surface.

The surface shear over the entire afterbody is presented in Figure 13. The $\theta = 0$ ordinate indicates the upper meridian plane and the $\theta = 180^\circ$ represents the lower. This picture reveals the flow structure in remarkable clarity over the two sliced surfaces where the flowstream expands rapidly toward the meridian plane. However, the flow over the conic section ($45^\circ \leq \theta \leq 135^\circ$) possesses no swirling motion. On top of the upper sliced surface, which is followed by the 20° compression flap, the expansion outward to the conic section of the body and the expansion inward to the meridian plane stands out. Three-dimensional phenomena are clearly evident. Reversed flow is indicated at the junction of the sliced surface and the compression flap. In an enlarged streamwise velocity distribution plot in the meridian plane (Figure 14), the reversed flow is embedded in an extremely small domain.

In the last figure, Figure 15, the cross-flow velocity distribution due to the configuration asymmetry is presented. The cross-flow velocity components are given in radial and tangential components. This picture not

only reinforces the observations made in the surface shear pattern but also reveals the drastic stream particle path variation across the boundary layer. The stream deflection from the surface changes rapidly across the boundary layer until emerging into the entropy layer.

SECTION VI

CONCLUSIONS

The numerical simulation of flow over a biconic body with a compression flap is successfully accomplished at a Mach number of 7.97, a Reynolds number of 9.228 million and at a zero degree angle of attack. The numerical results duplicate all the experimental measurements in pressure, pitot pressure and heat transfer within a few percent. The numerical results simulate the intricate flow field structure around a three-dimensional configuration.

The application of the MacCormack's implicit algorithm indicates the procedure is easily vectorized for large-scale data processing, and a significant gain in computer resources is realized. However, continuous research efforts to achieve a greater numerical efficiency are still needed.

REFERENCES

1. Lomax, H., "Some Prospect for the Future of Computational Fluid Dynamics," AIAA J., Vol. 20, No. 8, pp 1033-1043, 1982.
2. MacCormack, R.W., "The Effect of Viscosity in Hypervelocity Impact Cratering," AIAA Paper 69-354, Cincinnati, OH, 31 April-2 May 1969.
3. MacCormack, R.W., "Numerical Methods for Solving the Equations of Compressible Viscous Flow," AIAA J., Vol. 20, No. 9, September 1980, pp 1275-1281.
4. Knight, Doyle D., "A Hybrid Explicit-Implicit Numerical Algorithm for the Three-Dimensional Compressible Navier-Stokes Equations," AIAA Paper 83-0223, AIAA 21st Aerospace Sciences Meeting, 10-13 January 1983, Reno, NV.
5. Shang, J.S., "Implicit-Explicit Method for Solving the Navier-Stokes Equations," AIAA J., Vol. 16, No. 5, May 1978, pp 496-502.
6. Thompson, J.F., editor, "Numerical Grid Generation," Elsevier Science Publishing Co., Inc., New York, NY, 1982.
7. Coutler, S.M. and Carver, D.B., "Heat Transfer Surface Pressure and Flow Field Surveys on the AEDC Biconic and Slices and Flaps at Mach 8-MAT Phase J," AEDC-TR-81-V24, July 1981.
8. Shang, J.S., "Numerical Simulation of Wing-Fuselage Aerodynamic Interference," AIAA 83-225, AIAA 21st Aerospace Sciences Meeting, 10-13 January 1983, Reno, NV.
9. Baldwin, B.S. and Lomax, H., "Thin Layer Approximation and Algebraic Model for Separated Turbulent Flows," AIAA Paper 78-257, AIAA 16th Aerospace Sciences Meeting, 16-18 January 1978, Huntsville, AL.
10. Eiseman, P.R. and Smith, R.E., "Mesh Generation Using Algebraic Techniques," NASA Conf. Publication 2166, NASA Langley Research Center, Hampton, VA, 1980, pp 73-120.

11. MacCormack, R.W. and Baldwin, B.S., "A Numerical Method for Solving the Navier-Stokes Equations with Application to Shock-Boundary Layer Interaction," AIAA Paper 75-1, AIAA 13th Aerospace Sciences Meeting, 20-22 January 1975, Pasadena, CA.
12. Shang, J.S. and Hankey, W.L., "Numerical Solution for Supersonic Turbulent Flow Over a Compression Ramp," AIAA J., Vol. 13, No. 10, October 1975, pp 1368-1374.
13. Hung, C.M. and MacCormack, R.W., "Numerical Solutions of Three-Dimensional Shock Wave and Turbulent Boundary Layer Interaction," AIAA J., Vol. 16, 1978, pp 1090-1096.
14. Schiff, L.B. and Steger, J.L., "Numerical Simulation of Steady Supersonic Viscous Flow," AIAA J., Vol. 18, No. 12, December 1980, pp 1421-1430.
15. Lubard, S.C. and Hellwell, W.S., "Calculation of Flow on a Cone at High Angle of Attack," AIAA J., Vol. 12, No. 7, June 1974, pp 965-974.
16. Harris, T.B., "An Efficient Method for Supersonic Viscous Flow Field Calculations," AIAA Paper 83-0222, AIAA 21st Aerospace Sciences Meeting, 10-13 January 1983, Reno, NV, and private communication.

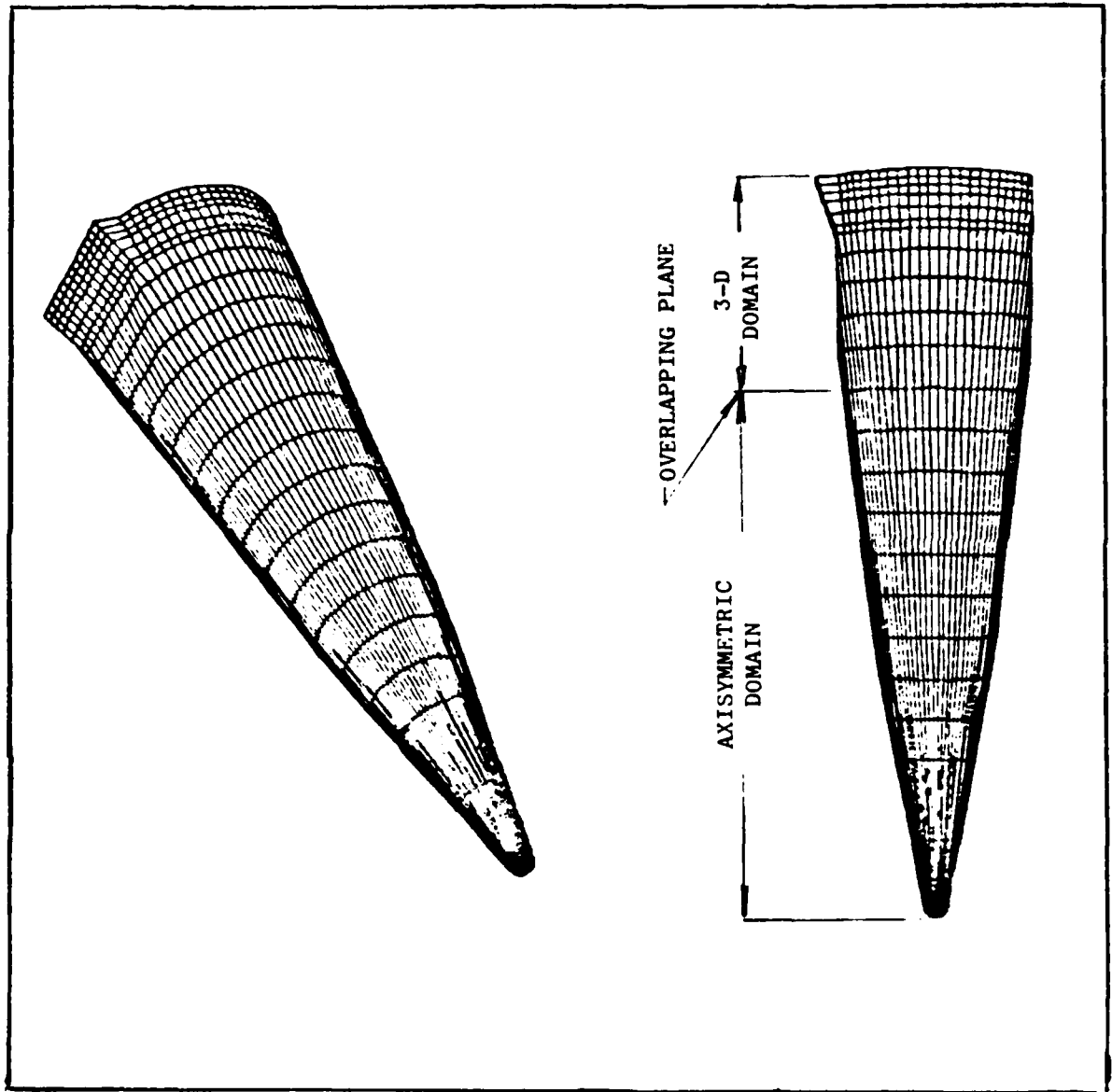


Figure 1 Schematic of the Biconic Configuration with Compression Flap

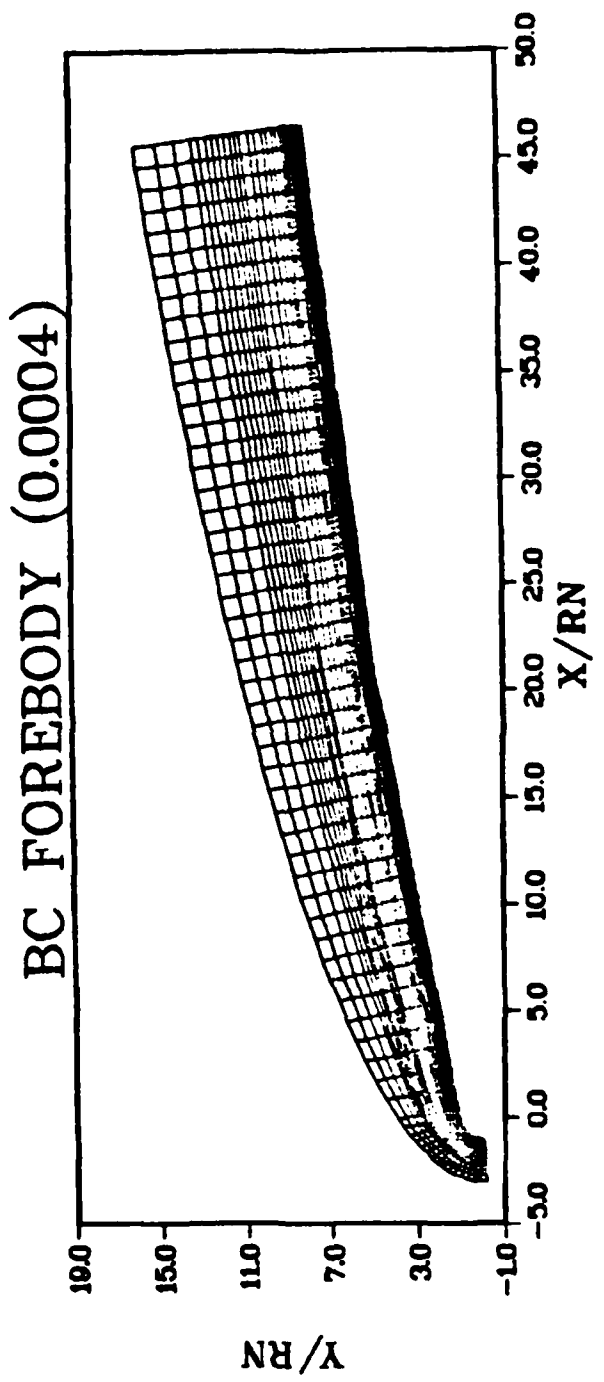


Figure 2 Mesh System of the Biconic Forebody

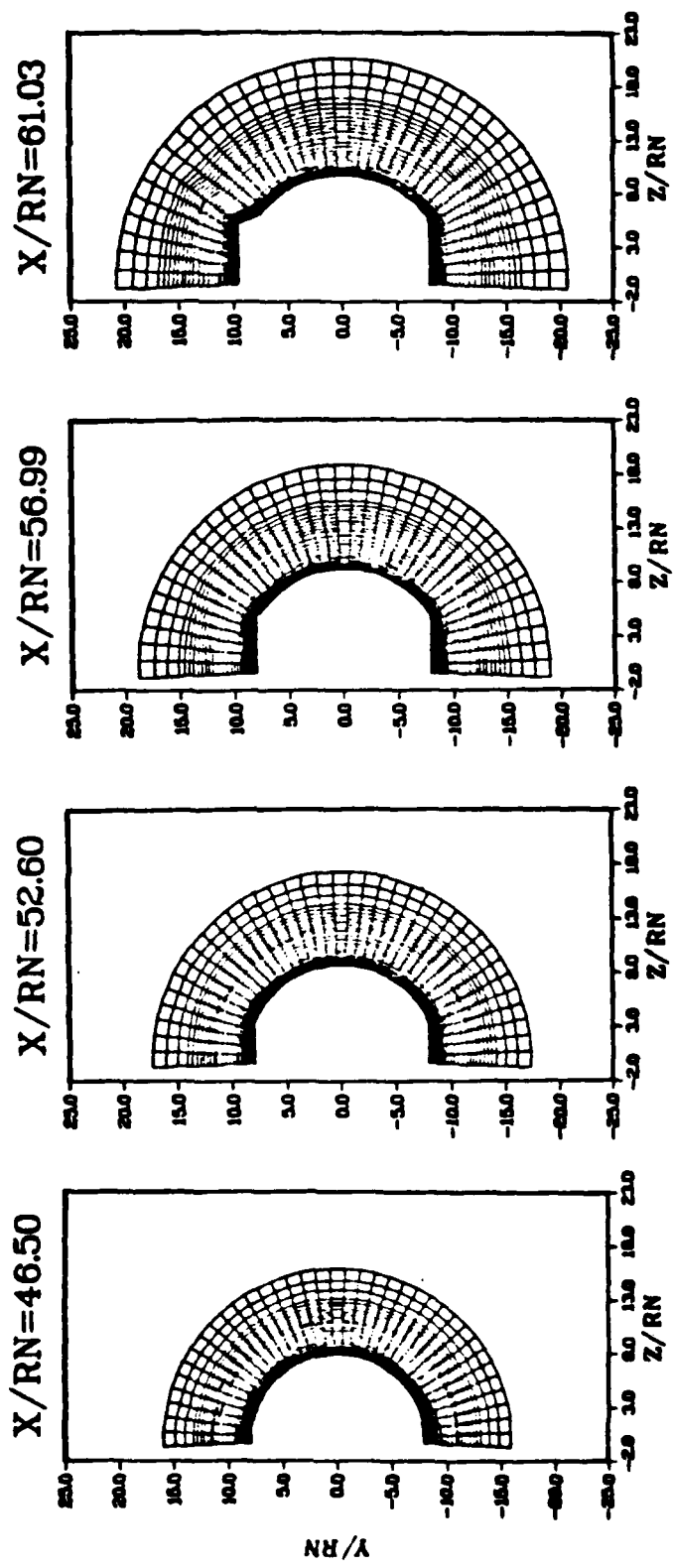


Figure 3 Mesh System of the Biconic Forebody

SURFACE PRESSURE

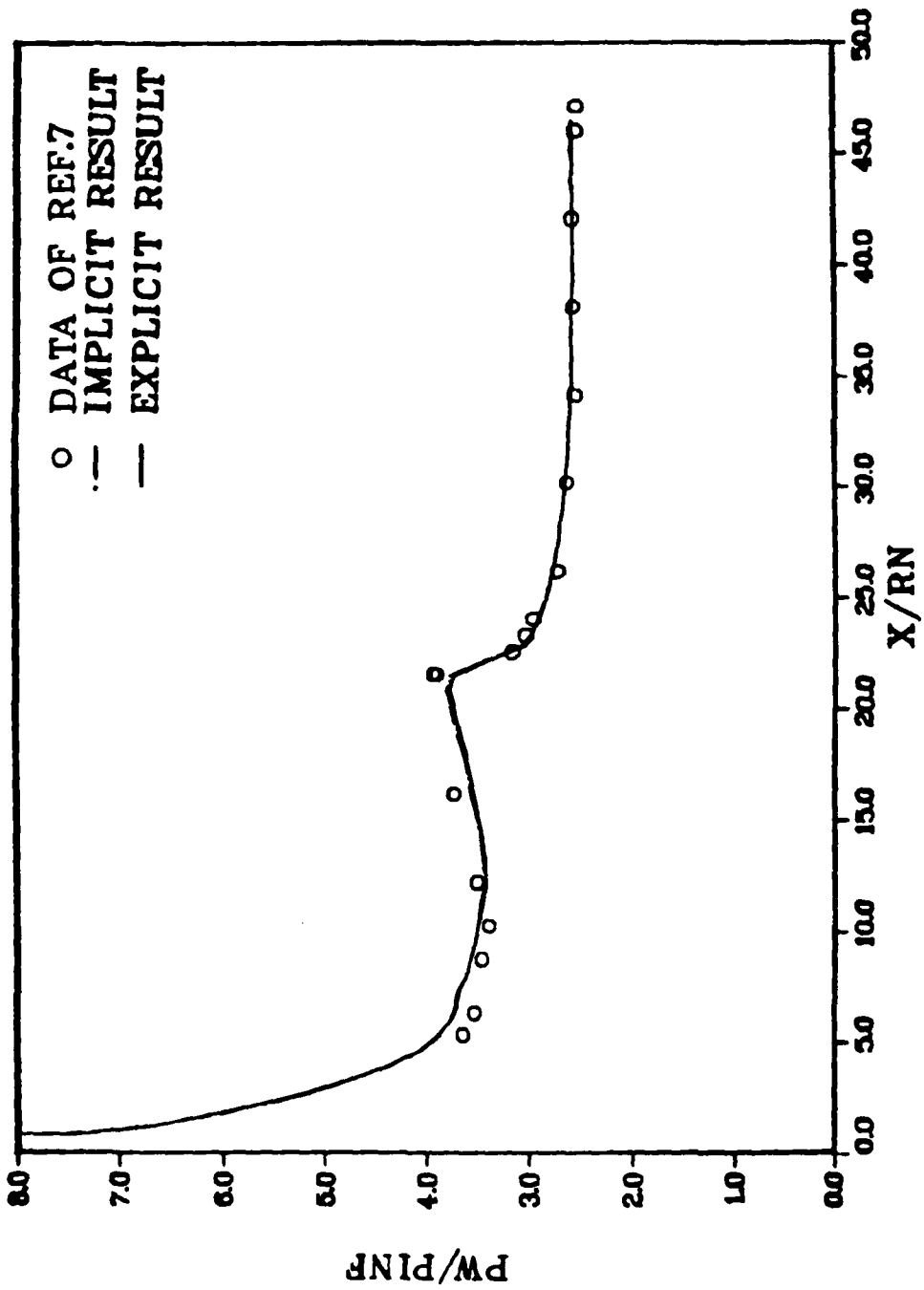


Figure 4 Comparison of the Surface Pressure Distributions on the Forebody

STATION NUMBER DISTRIBUTION

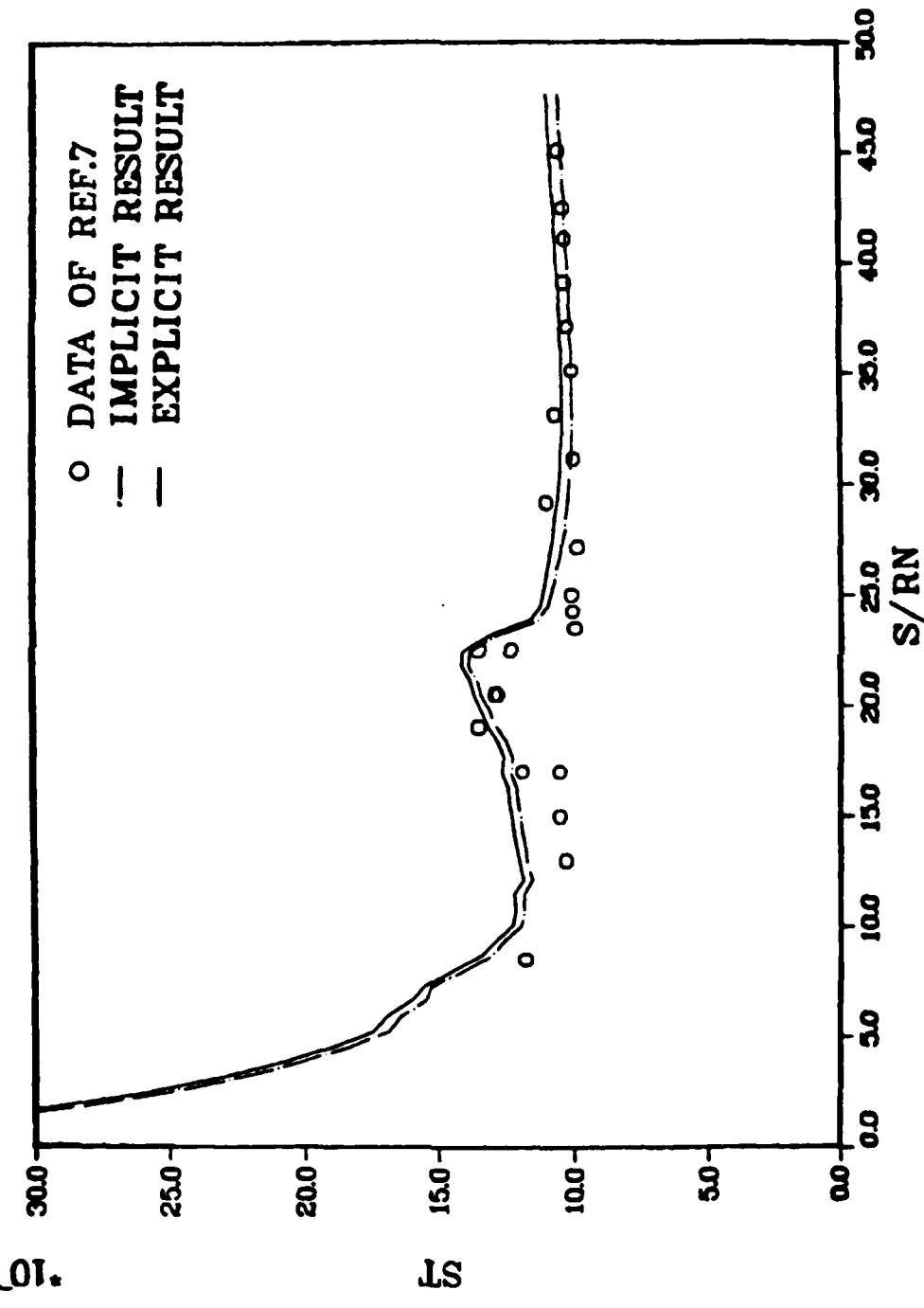


Figure 5 Comparison of Heat Transfer on Forebody

PITOT PRESSURE PROFILE

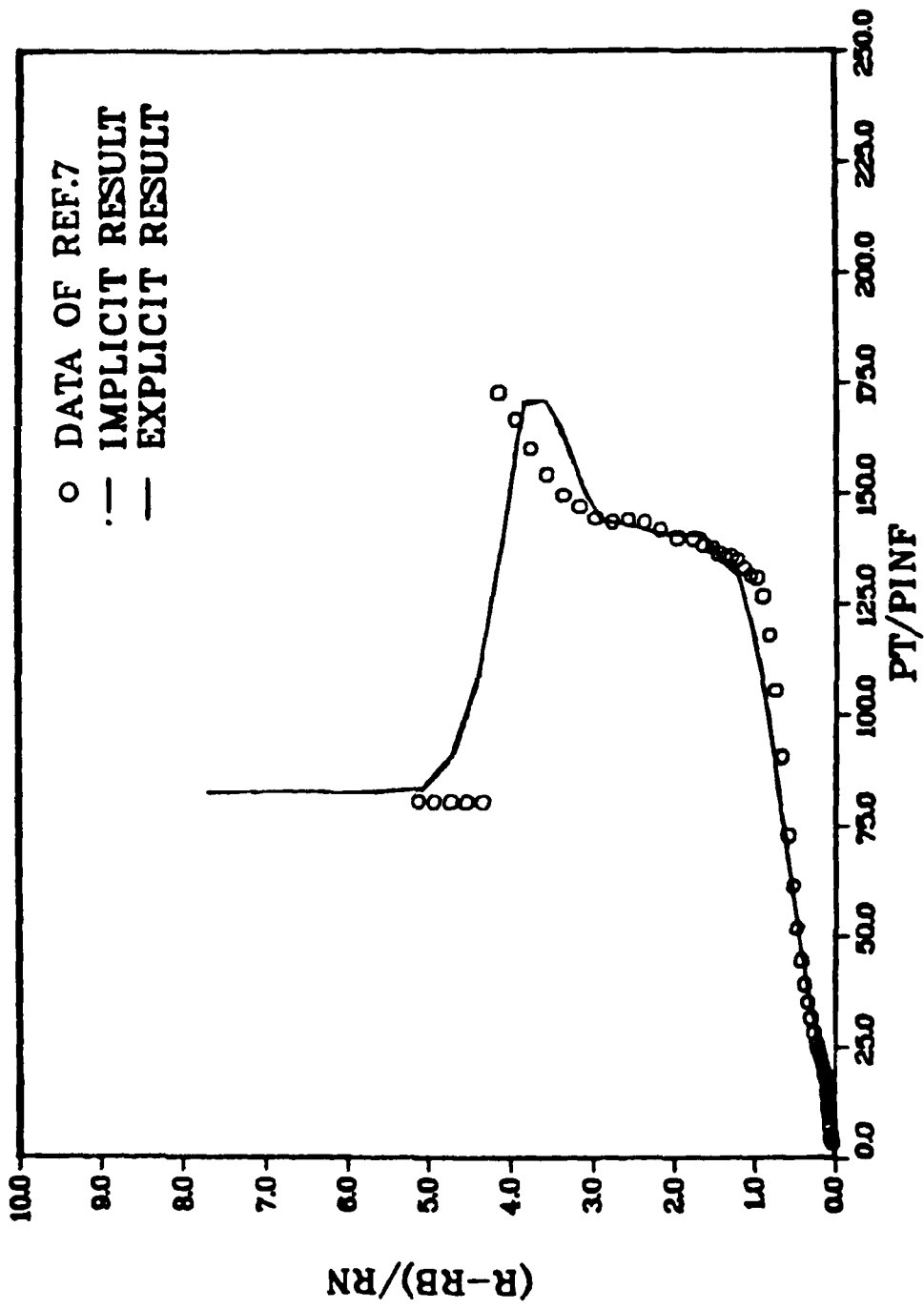


Figure 6 Comparison of Pitot Pressure Profile, $X/R_n = 41.45$

TANGENTIAL VELOCITY PROFILE

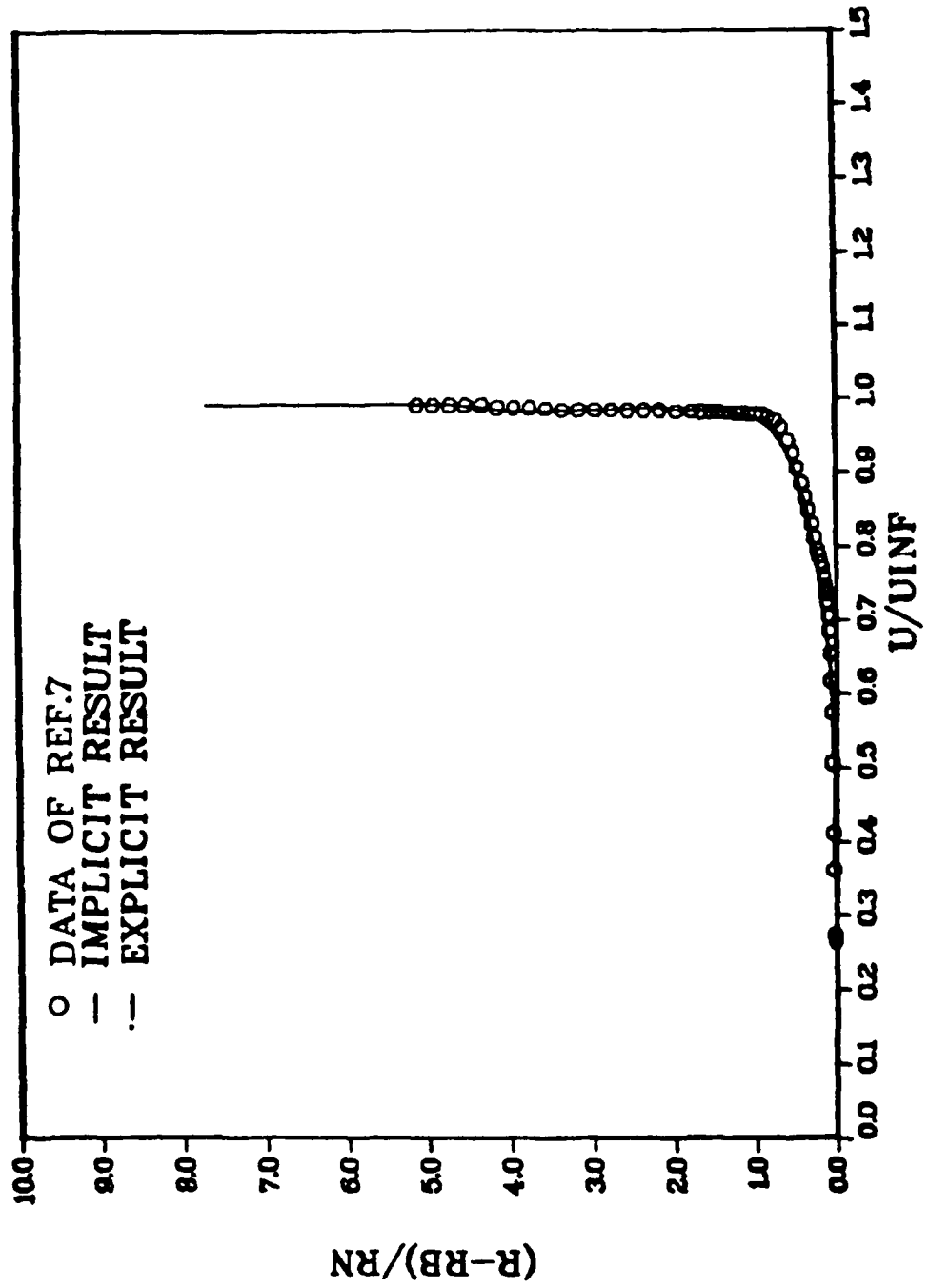


Figure 7 Comparison of Tangential Velocity Profiles ($X/Rn = 41.45$)

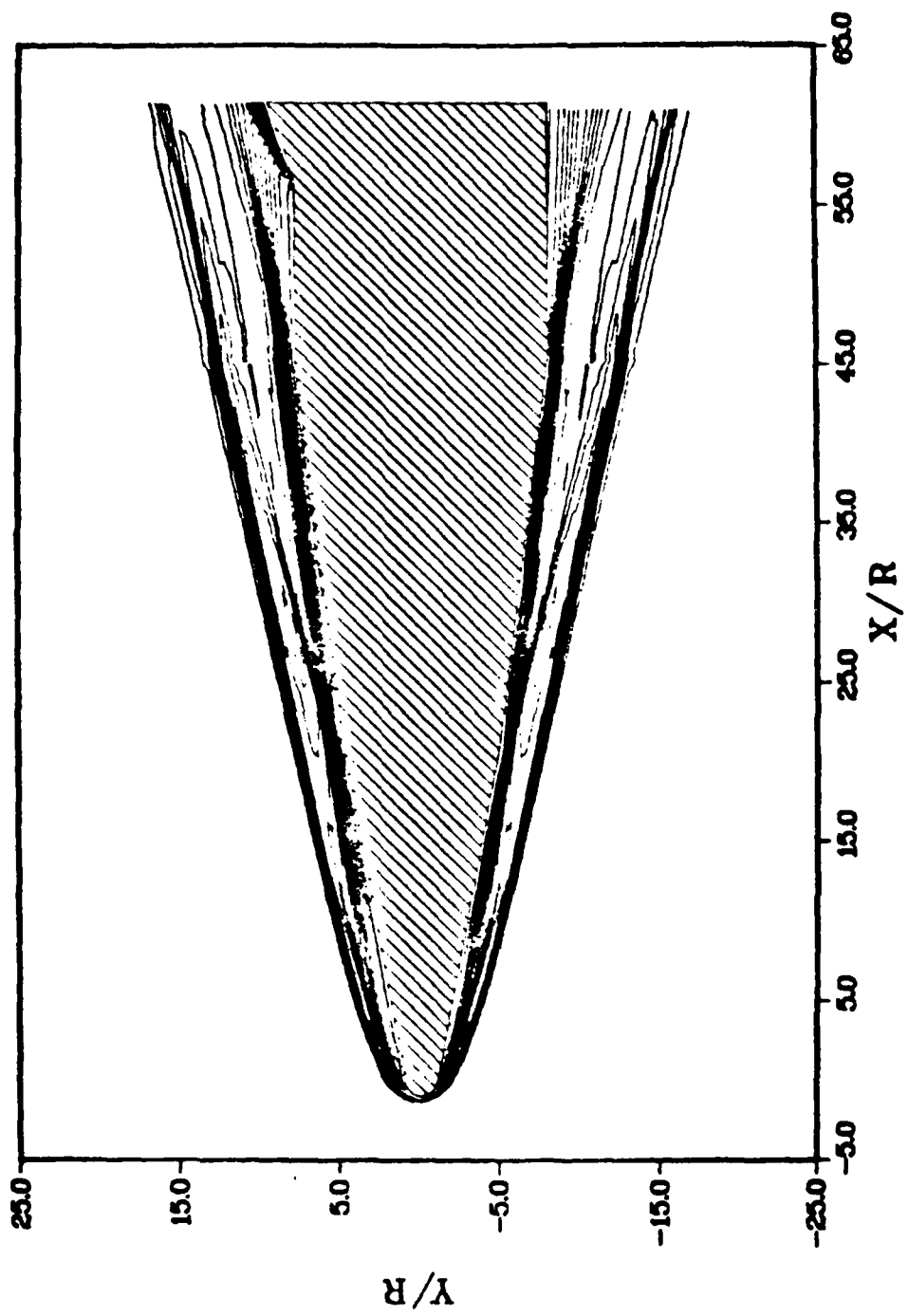


Figure 8 Density Contour in Meridian Plane

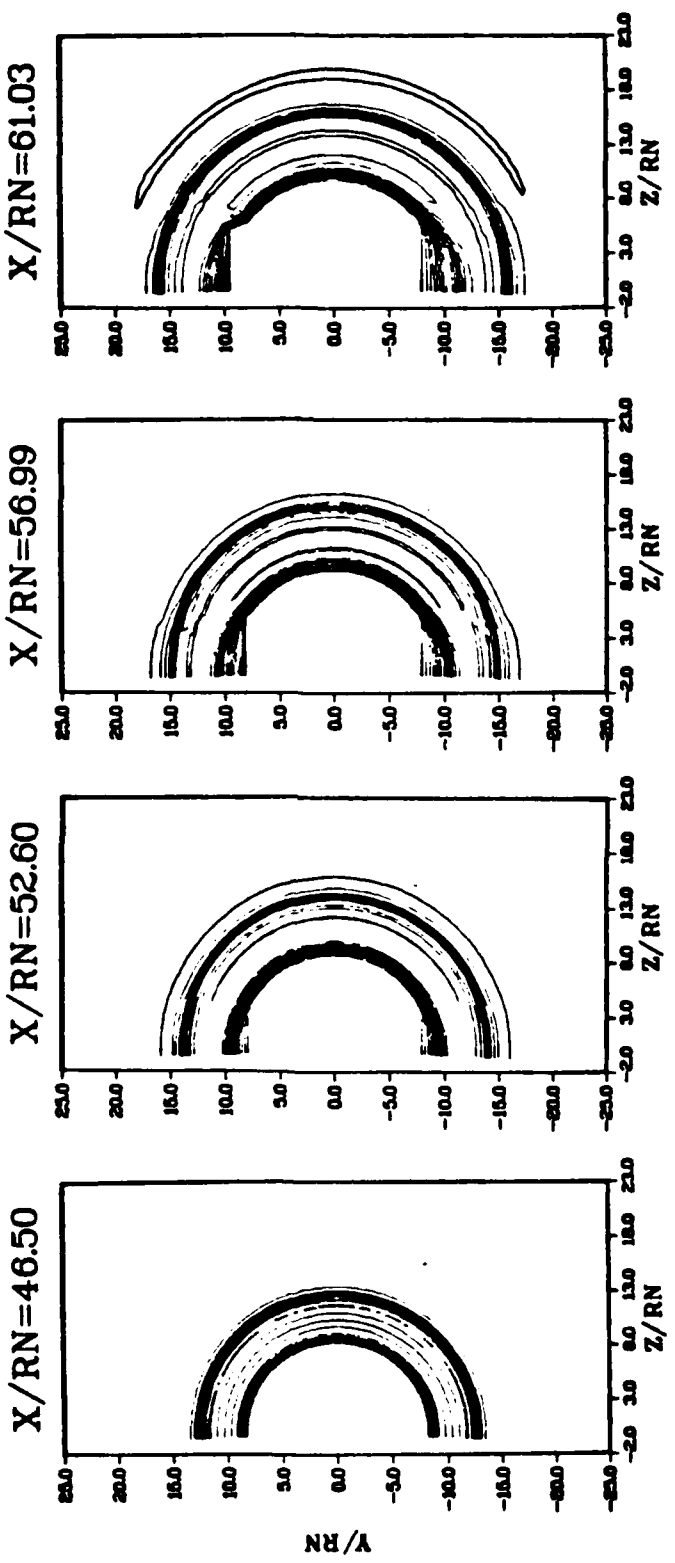


Figure 9 Density Contours in Cross-
Sectional Planes

SURFACE PRESSURE DISTRIBUTION

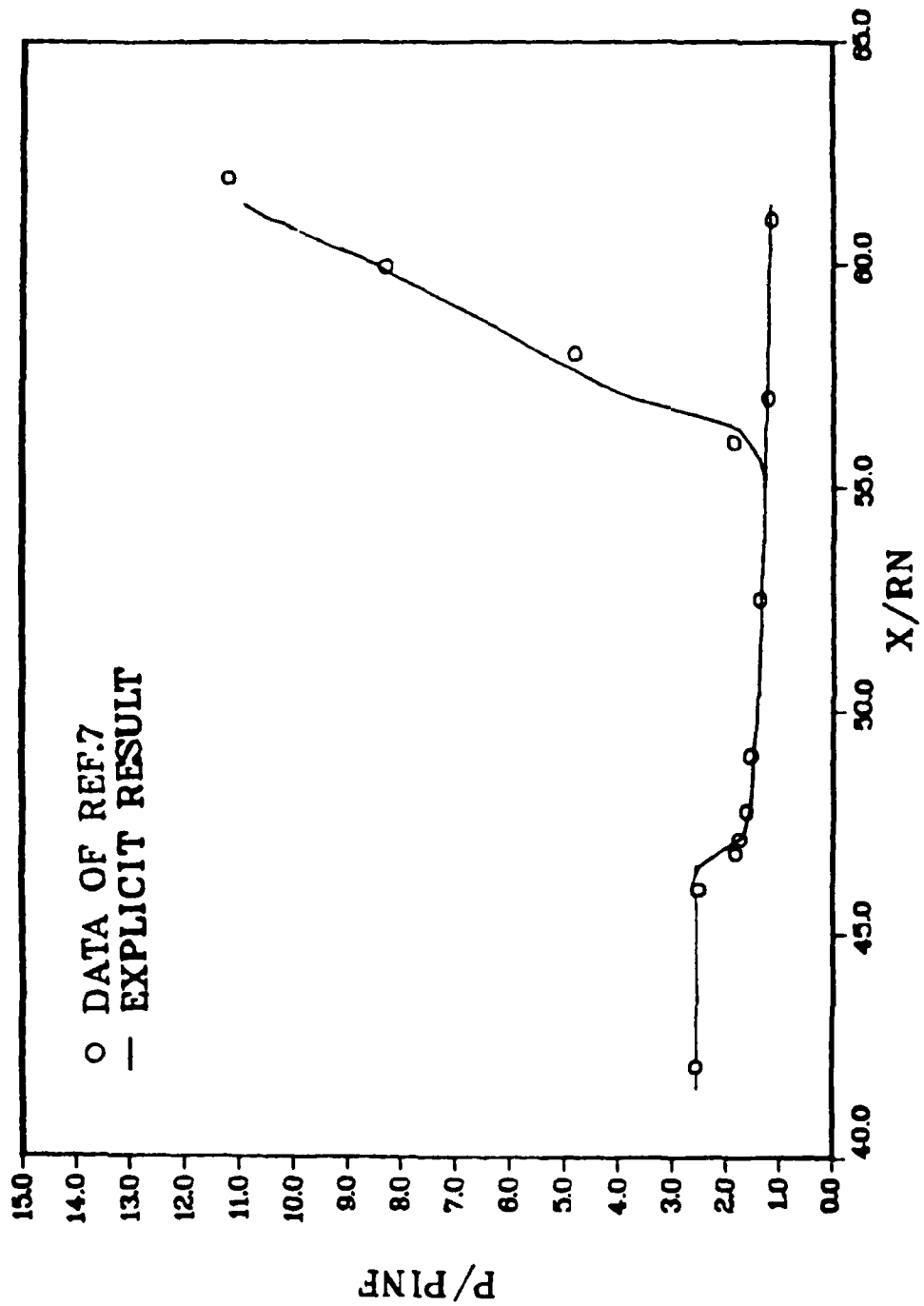


Figure 10 Surface Pressure Distributions
in Meridian Plane

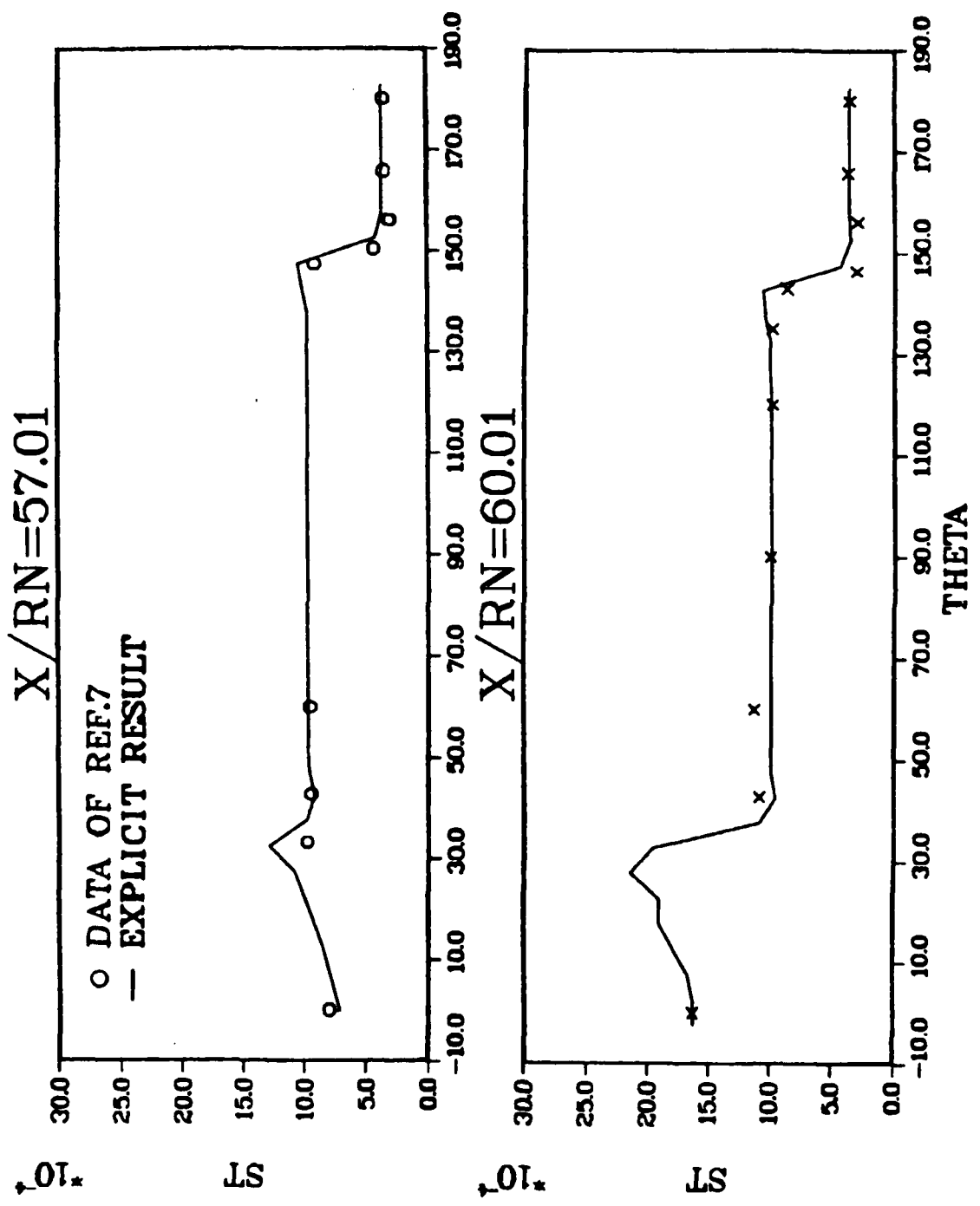


Figure 11 Comparison of Circumferential Stanton Number Distributions

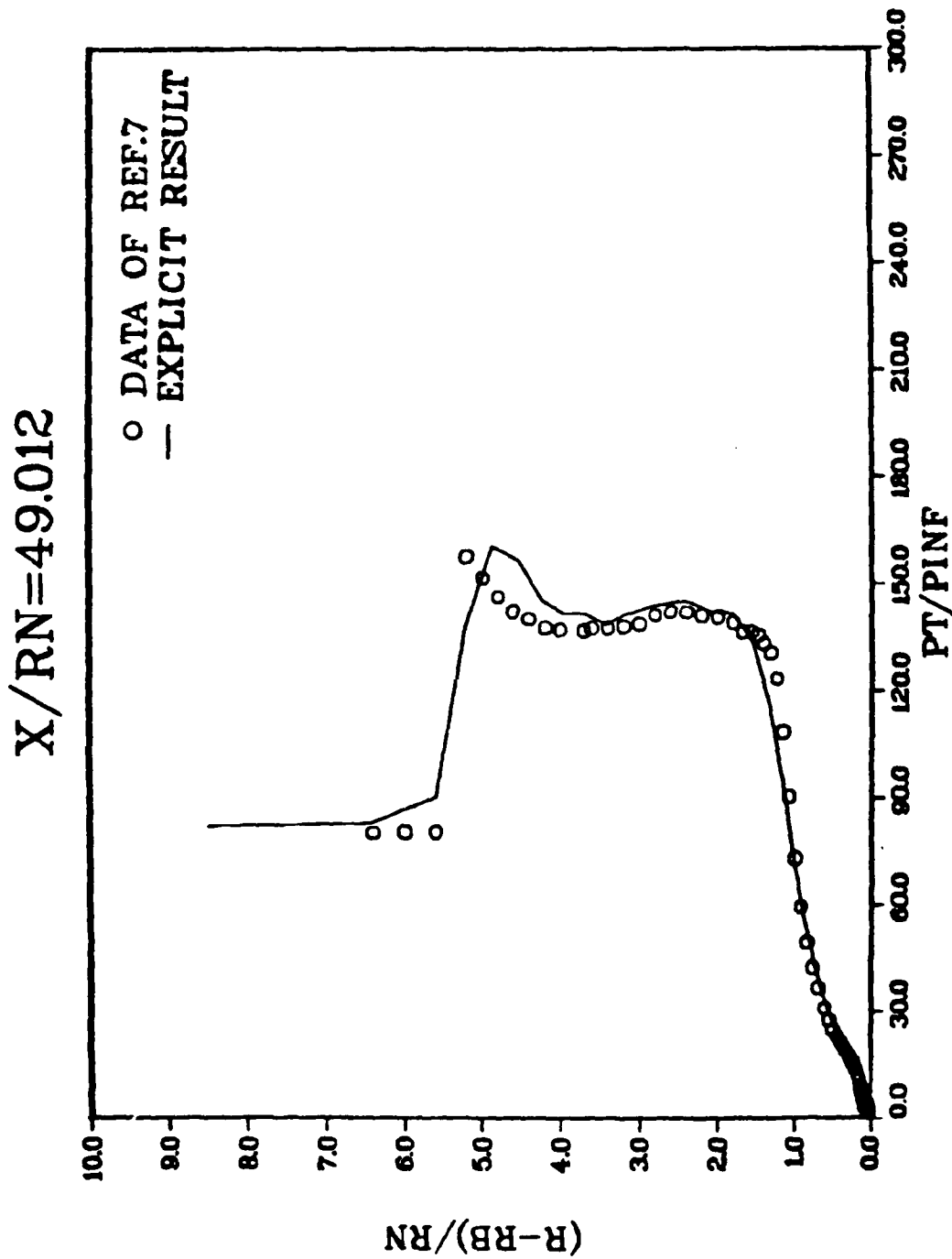


Figure 12 Comparisons of Pitot Pressure Profiles

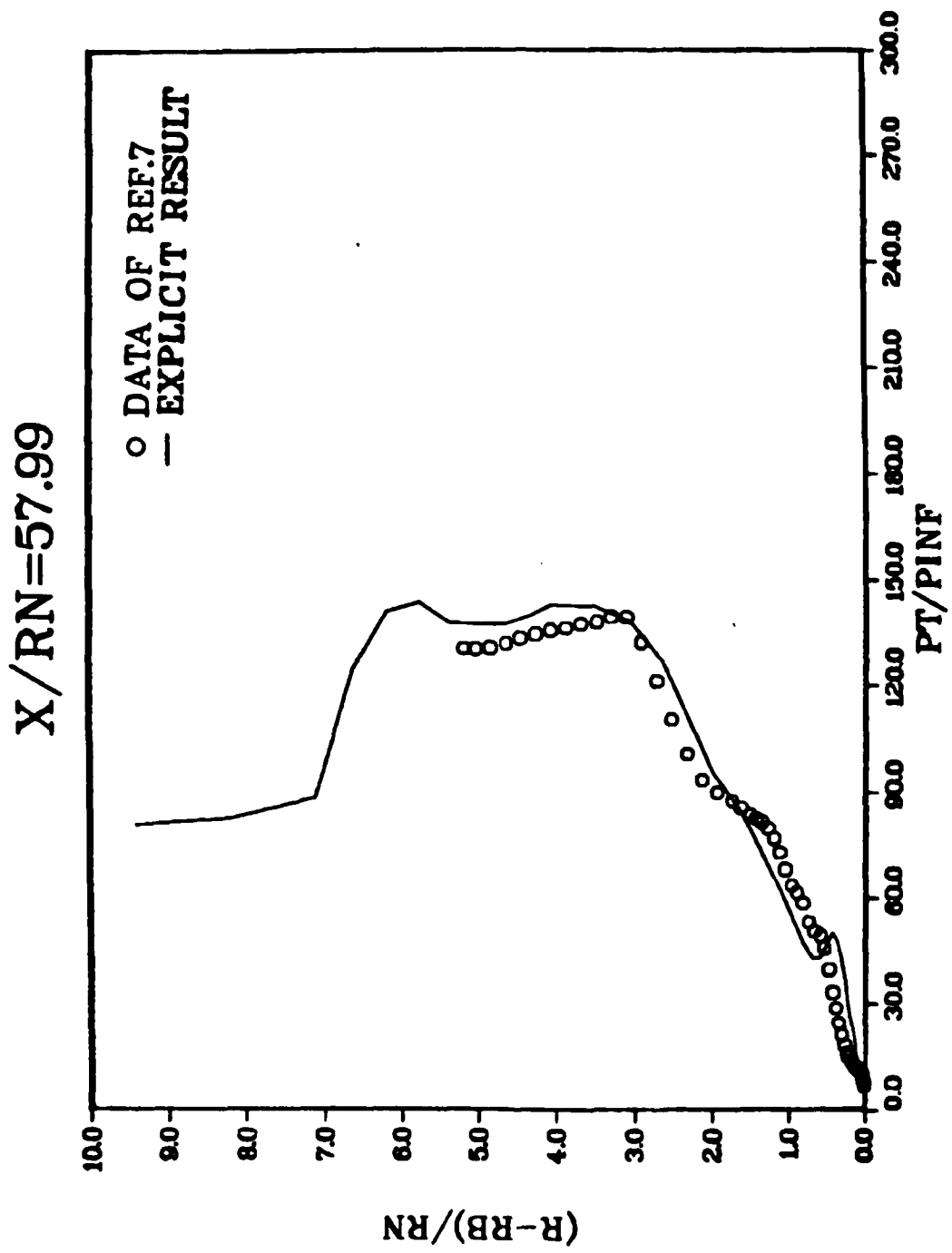


Figure 12 Comparisons of Pitot Pressure Profiles (Continued)

$X/RN = 61.928$

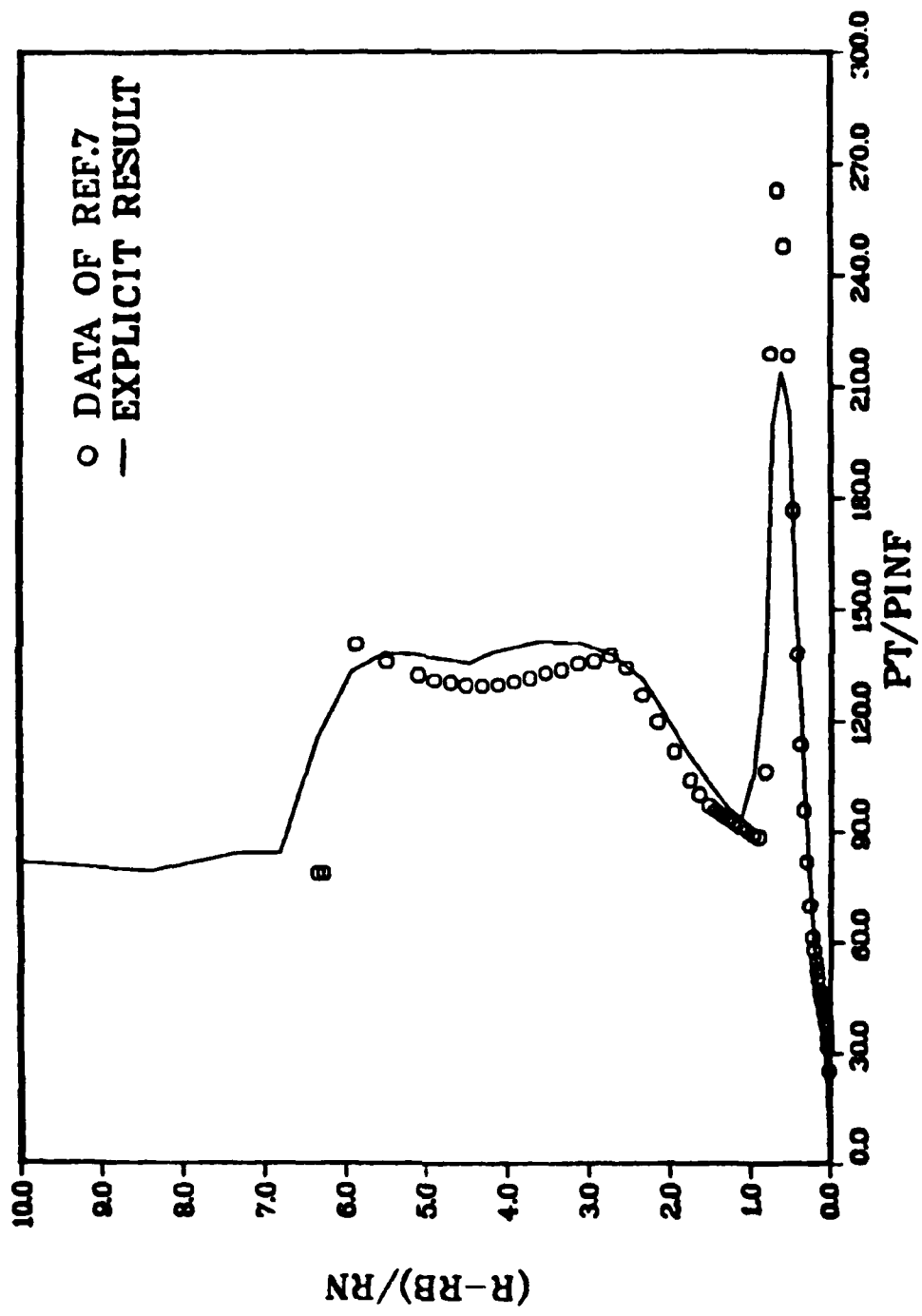


Figure 12 Comparisons of Pitot Pressure Profiles (Continued)

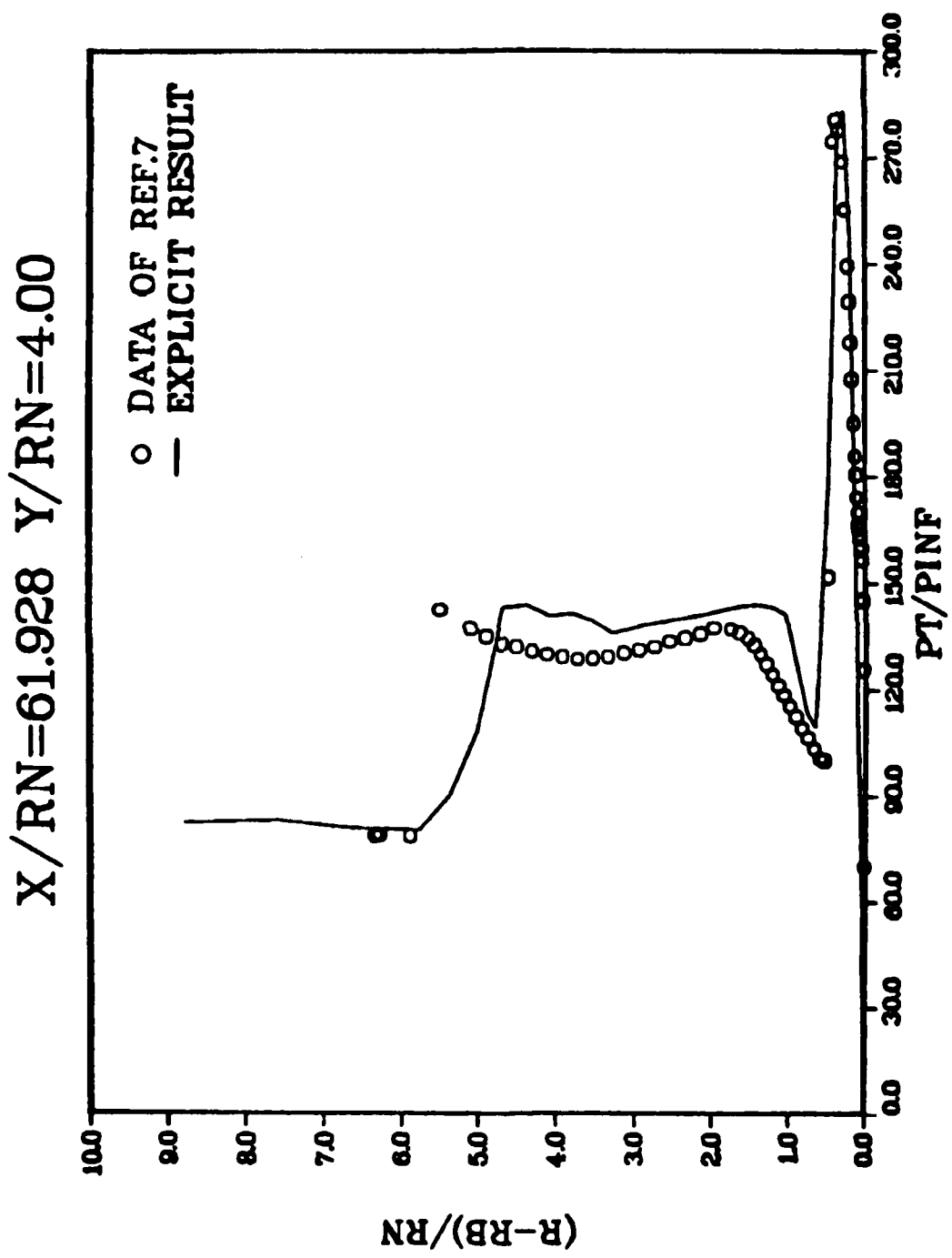


Figure 12 Comparisons of Pitot Pressure Profiles (Concluded)

SURFACE SHEAR PATTERN

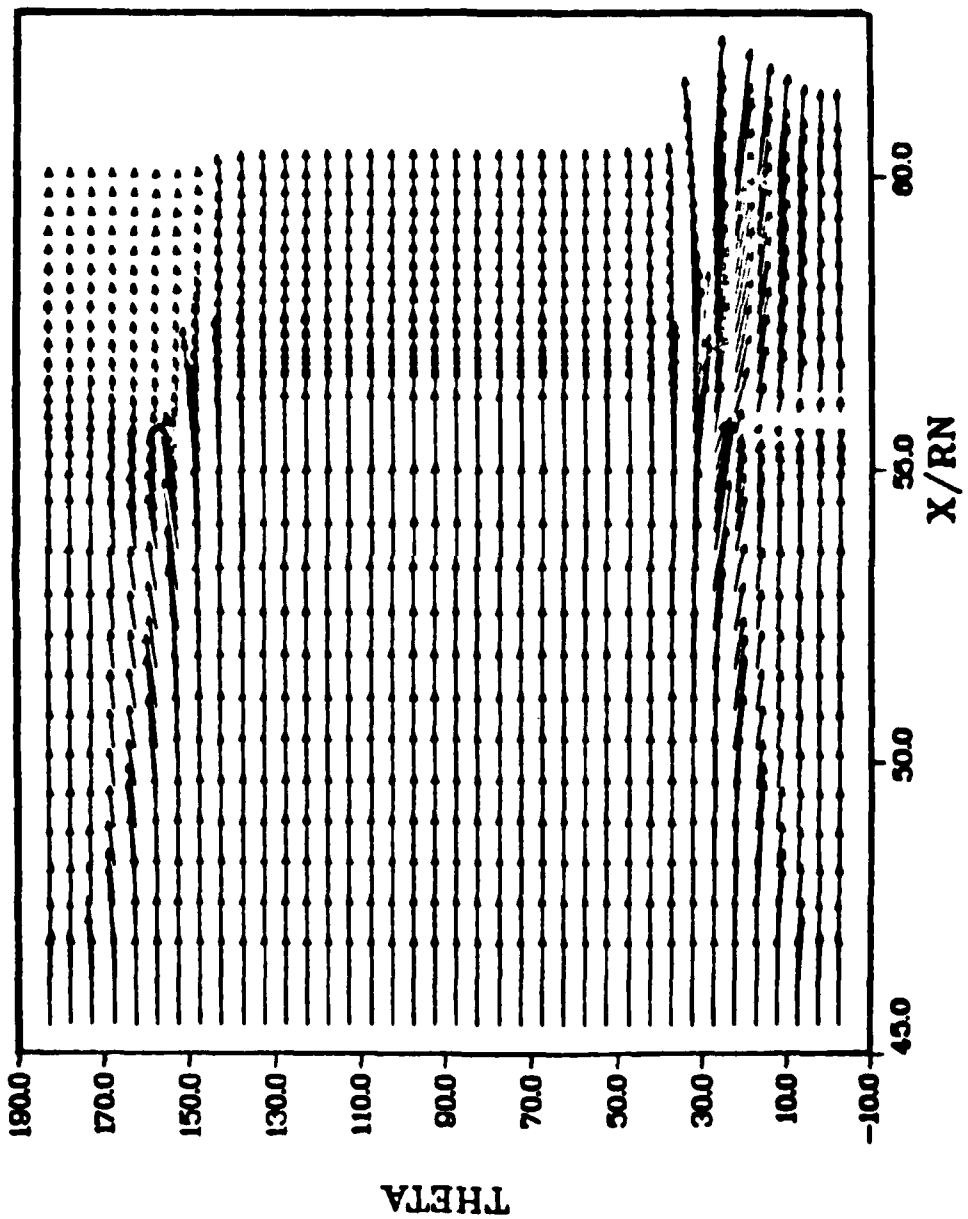


Figure 13 Surface Shear Pattern of the Afterbody

VELOCITY PROFILE IN MERIDIAN PLANE

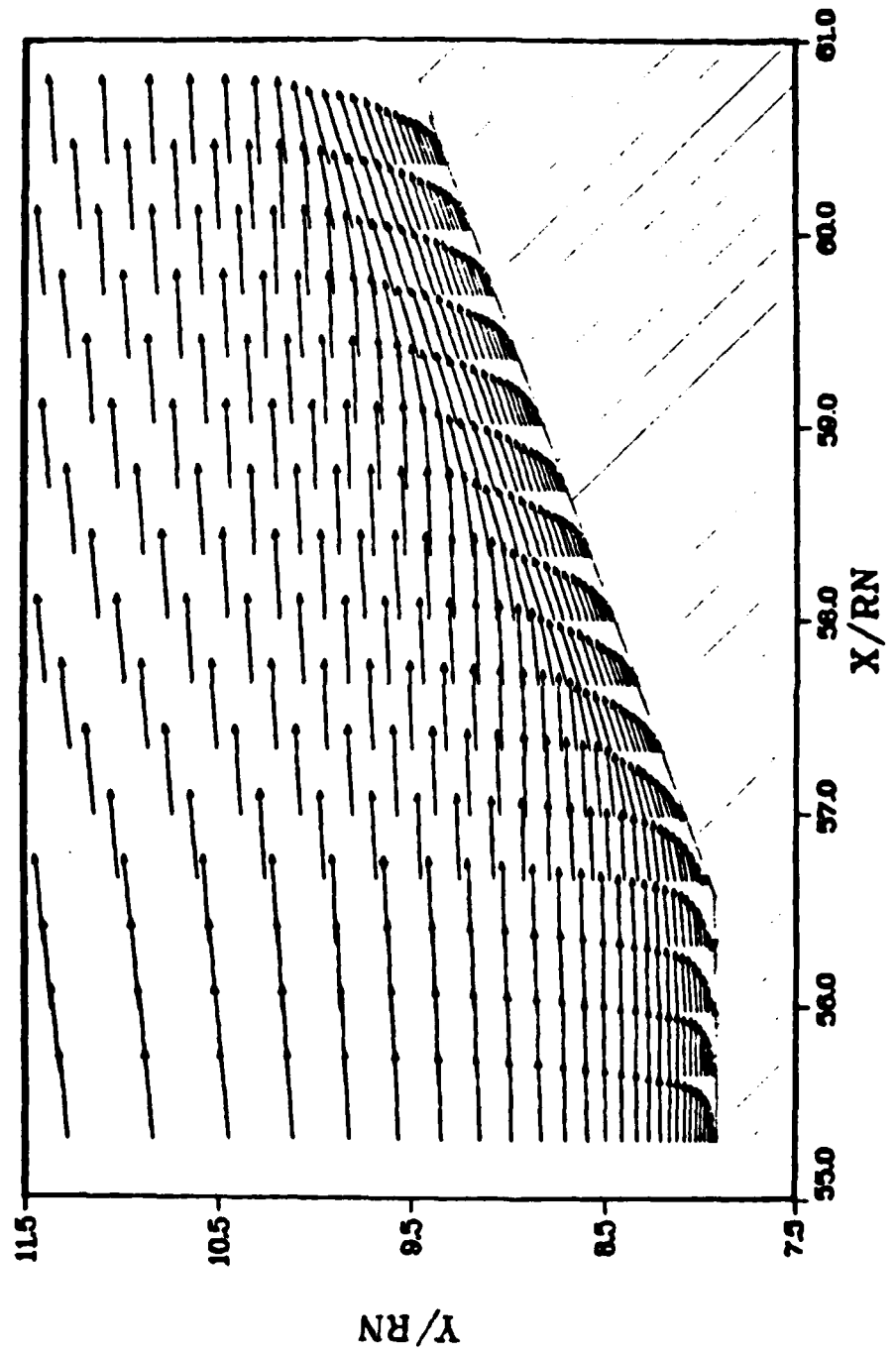


Figure 14 Velocity Field Over the
Compression Flap

CROSSFLOW VEL DISTRIBUTION ($X/RN=61.03$)

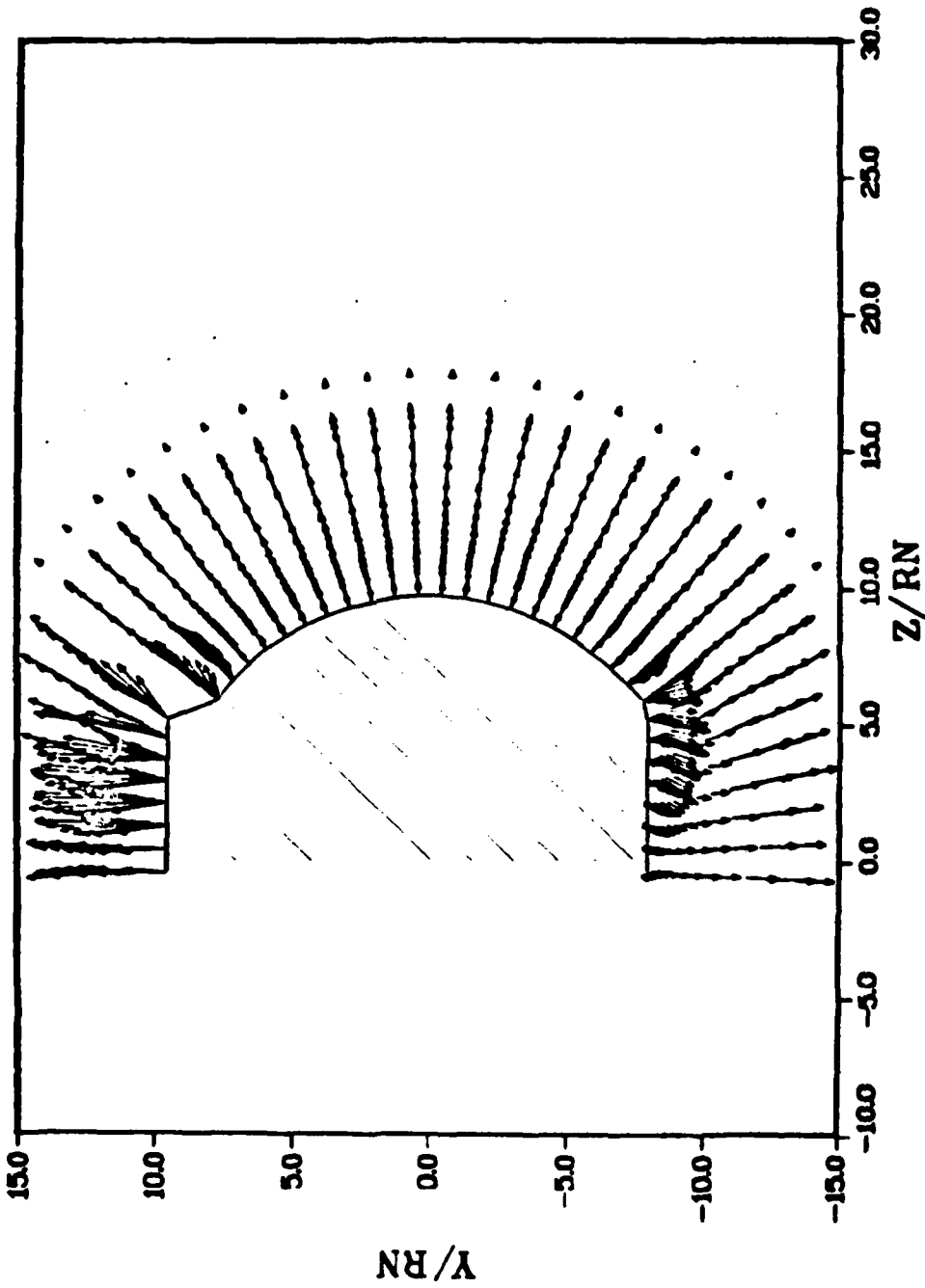


Figure 15 Cross-Flow Velocity Distribution, ($X/Rn = 61.03$)

END

FILMED

4-85

DTIC